



Article

Numerical Study on Non-Icebreaking Ship Maneuvering in Floating Ice Based on Coupled NDEM–MMG Modeling

Deling Wang¹, Luyuan Zou¹ , Zhiheng Zhang^{1,2,*}  and Xinqiang Chen³ ¹ Merchant Marine College, Shanghai Maritime University, Shanghai 201306, China; dlwang@shmtu.edu.cn (D.W.); zouluyuan01@163.com (L.Z.)² State Key Laboratory of Ocean Engineering, Shanghai Jiao Tong University, Shanghai 200240, China³ Institute of Logistics Science and Engineering, Shanghai Maritime University, Shanghai 201306, China; chenxinqiang@stu.shmtu.edu.cn

* Correspondence: zhzhzhang@shmtu.edu.cn

Abstract

The maneuvering performance of ships in marginal ice zones is critical for navigational safety, yet most existing studies focus on icebreaking vessels. This study develops a coupled numerical framework that integrates the Non-Smooth Discrete Element Method (NDEM) for simulating ship–ice interactions with the three-degree-of-freedom MMG model for ship dynamics. The framework was applied to an S175 container ship, and numerical simulations were conducted for turning circle and Zig-Zag maneuvers under varying ice concentrations (0–60%), floe sizes, and rudder angles. NDEM efficiently handles complex, high-frequency multi-body collisions with larger time steps compared to conventional DEM or CFD–DEM approaches, enabling large-scale simulations of realistic ice conditions. Results indicate that increasing ice concentration from 0% to 60% reduces the turning diameter from 4.11L to 3.21L and decreases steady turning speed by approximately 53%. Larger floes form stable force chains that restrict lateral motion, while higher rudder angles improve responsiveness but may induce dynamic instability. These findings improve understanding of non-icebreaking ship maneuverability in ice and provide practical guidance for safe and efficient Arctic navigation.

Keywords: maneuvering performances; broken ice; ship-ice interaction; MMG model

Academic Editor: Diego Villa

Received: 5 July 2025

Revised: 8 August 2025

Accepted: 14 August 2025

Published: 17 August 2025

Citation: Wang, D.; Zou, L.; Zhang, Z.; Chen, X. Numerical Study on Non-Icebreaking Ship Maneuvering in Floating Ice Based on Coupled NDEM–MMG Modeling. *J. Mar. Sci. Eng.* **2025**, *13*, 1578. <https://doi.org/10.3390/jmse13081578>

Copyright: © 2025 by the authors. Licensee MDPI, Basel, Switzerland. This article is an open access article distributed under the terms and conditions of the Creative Commons Attribution (CC BY) license (<https://creativecommons.org/licenses/by/4.0/>).

1. Introduction

In the context of global climate warming, the rapid decline in Arctic sea ice has made the development of Arctic shipping routes increasingly feasible [1]. Among them, the Northern Sea Route (NSR) offers a voyage approximately 40% shorter than the traditional Suez Canal route, which presents significant economic and societal advantages and has promise as a vital trade corridor connecting Europe, North America, and Asia. However, Arctic navigation faces a major challenge posed by sea ice conditions, particularly the impact of floating ice on ship maneuverability, which has become a focal point in polar navigation research.

With the expansion of floating ice coverage, many conventional merchant ships not designed with icebreaking capabilities have gradually begun operating in Arctic waters with varying ice densities and thicknesses. Unlike purpose-built icebreakers, these non-icebreaking ships typically possess only limited structural reinforcement against ice and lack active icebreaking functionality. When navigating through floating ice regions, such ships must frequently adjust their maneuvering state to identify optimal routes, thereby

maximizing fuel efficiency and improving economic performance. However, compared to ice-free waters, floating ice conditions significantly impair the maneuverability of non-icebreaking vessels. Specific challenges include difficulty in heading control, delayed steering responses, and a greater tendency to drift passively in areas of high ice concentration. Once surrounded by floating ice, these ships may lose maneuvering capability entirely, facing considerably higher navigational risks than icebreakers. Currently, most research on polar ship performance focuses on icebreaking vessels, while studies on the maneuvering performance of non-icebreaking ships in floating ice environments remain scarce. Therefore, it is of substantial practical importance to investigate the maneuverability of non-icebreaking ships under such conditions. This study establishes a numerical simulation model tailored to simulate the maneuvering motion of non-icebreaker vessels in floating ice regions. The objective is to systematically explore the effects of different ice conditions on ship maneuverability, providing a theoretical foundation for safety assessment and the optimization of navigation strategies for non-icebreaking ships operating in floating ice zones.

With the rapid growth of polar navigation, the maneuvering performance of ships in ice-covered waters has emerged as a critical research topic. In parallel, recent studies across the broader maritime science domain have underscored the increasing importance of advanced numerical models and intelligent systems in addressing operational and environmental challenges in shipping [2–6]. Such modeling and simulation methodologies have also been widely applied to ship hydrodynamics and maneuvering prediction, providing valuable tools for understanding complex marine environments. To reduce experimental costs and improve research efficiency, many scholars have adopted numerical methods to investigate the resistance and motion behavior of ships in ice-infested regions. Among these efforts, accurately modeling the interaction between the ship hull and ice remains the central challenge for achieving reliable maneuvering simulations in ice-covered waters. Currently, commonly used modeling approaches include empirical models, mechanical models, finite element methods (FEM), and discrete element methods (DEM), among others.

Empirical models estimate ice resistance based on extensive experimental or observational data, typically using regression analysis or semi-empirical formulations. For example, early resistance formulas developed for ships operating on level ice have been widely used for resistance prediction under such conditions, offering a convenient means of rapid performance evaluation during the preliminary design stage [7–9]. The prediction of ice resistance in broken ice conditions is more complex than that in level ice, as it involves a greater number of influencing factors. Based on Colbourne’s dimensionless analysis method, Jeong et al. [10] derived an empirical formula for the resistance to broken ice that incorporates the effect of channel width, using the test results of the model of the icebreaker “Araon”. These models are simple to implement and highly practical. However, their applicability is generally limited to the range of data used for calibration and cannot be easily extended to complex ice environments. Furthermore, empirical formulas often do not capture the influence of hull geometry on ice loads. Therefore, during the detailed design phase, model tests are still required to correct and validate the simulation results [11].

In contrast, mechanical models are developed based on the principles of ice mechanics and failure mechanisms, providing a more physically grounded approach to ice force prediction. For example, such models can treat the ice sheet as a cantilever beam undergoing bending failure, or apply the Mohr–Coulomb criterion to assess crushing failure [12]. These models are capable of explicitly linking hull geometric parameters—such as bow flare angle and waterline entrance angle—to the resulting ice forces, offering a clearer physical interpretation. While mechanical models effectively explain the origins of ice loads under different breaking modes, the actual failure process of sea ice is complex and

varied. A single mechanical model typically captures only the dominant failure mode and is inadequate to represent the combined mechanisms. For example, Zhou et al. [13] considered only one type of ice failure during ship maneuvering simulations, overlooking the coupled effects of bending and crushing. In general, the applicability of mechanical models under complex ice conditions remains limited and additional validation through experimental observations is often required.

As a high-fidelity method for modeling continuous media, the Finite Element Method (FEM) has been widely applied in the simulation of ship–ice interactions, particularly suitable for investigating localized failure phenomena such as ice crushing and splitting [14]. For example, Kim et al. [15] employed the ABAQUS/explicit solver coupled with an Eulerian–Lagrangian approach to simulate ship–ice interactions in broken ice regions, comprehensively accounting for complex interactions among ice–sea, ice–ice and ice–structure interfaces. Wang et al. [16] used LS-DYNA to perform finite element simulations of ice loads on ships in fragmented ice fields, accurately capturing floe deformation and interactions, thus improving the accuracy of ice load prediction. Building on these efforts, Kim et al. [17] integrated ABAQUS/Explicit with the HydroQus plugin to systematically study the ice-breaking process of the Araon research vessel, analyzing in detail the influence of hydrodynamic forces and ship velocity on ice-breaking resistance and exploring ship responses, such as speed, pitch, and heave, under different ice-breaking scenarios. In addition, Xing et al. [18] employed a three-dimensional FEM combined with the cohesive element method to examine the distribution characteristics of ice loads at various structural interfaces. Despite the high accuracy and adaptability of FEM, its application at the full-ship scale is often constrained by high computational complexity and long simulation times.

In addition to the widely used finite element method (FEM), various other numerical methods have also been employed in ice–structure interaction studies, such as Smoothed Particle Hydrodynamics (SPH), Boundary Element Method (BEM), and meshless approaches like the Material Point Method (MPM). Makarov et al. [19] systematically analyzed these numerical methods in terms of computational efficiency, accuracy, and applicability for ice–structure interaction problems, highlighting their respective strengths and limitations. However, these approaches generally suffer from high computational costs and limitations in simulation scale, particularly in large-scale and high-frequency collision simulations relevant to ship maneuvering. Therefore, developing efficient and robust numerical methods capable of handling complex collision scenarios remains a crucial research challenge.

The Discrete Element Method (DEM) has increasingly become a dominant approach to predicting ice loads in broken ice scenarios, due to its ability to accurately simulate collisions and accumulation processes between ice floes and between ice and the ship hull. For example, Li et al. [20] modelled ice floes using three-dimensional disk elements and represented the hull of the ship with triangular elements, analysing variations in ice loads under different speed and ice conditions of the ship. Polojarvi et al. [21] extended this work to full-scale simulations, evaluating ship responses in broken ice fields of varying thickness and concentration, and highlighted the significant role of hydrodynamics in ice resistance. To further enhance the physical consistency and dynamic accuracy of ice modelling, recent studies have coupled DEM with Computational Fluid Dynamics (CFD), forming integrated CFD–DEM simulation frameworks [22]. This hybrid approach enables simultaneous modelling of ice floe contact and accumulation behaviours, as well as hydrodynamic effects such as ship-generated waves [23] and propeller-induced flow fields, making it one of the most promising methods for predicting ice load in floating ice environments [24]. Hu et al. [25] investigated the performance of non-icebreaker ships in the marginal ice zone (MIZ) using CFD-DEM simulations, comparing their predictions with

traditional empirical formulations. To improve the validation of the model and the applicability of engineering, some researchers integrated physical towing tank experiments with CFD-DEM simulations [26,27]. The former proposed a cost-effective method for evaluating broken ice resistance and verified the feasibility of simulating ice dynamics using synthetic non-freezing ice; the latter developed a self-propelled simulation model for propeller-ice interaction and validated its effectiveness for propulsion efficiency assessment against ice tank test data. Moreover, Zou et al. [28] used CFD-DEM to investigate the influence of broken ice channel width on coupled ship-ice-water responses. Their results showed that narrower channels lead to an increased accumulation of ice in the bow and midship regions, significantly increasing the resistance to ice and the lateral asymmetric loads. The study also revealed that ship-generated waves can effectively reduce collision frequency and contact intensity, thus alleviating ice resistance, a drag reduction effect that becomes more pronounced at higher ship speeds. Collectively, these studies demonstrate the capability of CFD-DEM to accurately predict ice resistance and lateral loads under complex ice conditions and broaden its potential for analysing the maneuverability of non-icebreaking ships in ice-infested waters. Traditional DEM calculates collision forces between ice floes and between ice and the hull by defining contact force-displacement relationships, such as spring-damper models. This allows for an effective simulation of the behaviour of ice accumulation, compaction, and movement. However, DEM faces significant computational bottlenecks when handling large-scale multi-contact systems. In scenarios involving frequent collisions or numerous ice floes, very small time steps are required to maintain numerical stability, leading to a substantial decline in computational efficiency.

To overcome these limitations, the Non-Smooth Discrete Element Method (NDEM) has been developed. Unlike classical DEM, NDEM treats contact as instantaneous, non-penetrative constraints and enforces non-penetration conditions by solving for impulse and constraint forces. This allows for stable simulations of complex multibody collision systems with significantly larger time steps. As such, NDEM is particularly well suited for modelling the frequent collisions and strong rigid-body coupling characteristic of ship motions in ice-covered waters. To validate the feasibility of NDEM in complex fluid-structure interaction scenarios, Mierke et al. [29] coupled a free surface flow solver based on the Lattice Boltzmann method (elbe) with the ODE rigid-body dynamics engine to simulate multiphase ship-ice interaction systems in marine environments. Lubbad & Løset [30] as well as van den Berg et al. [31] further developed numerical frameworks capable of real-time simulation of ship-ice contact processes and extended the NDEM technique to support hybrid contact modelling between compliant continua and rigid discontinuous bodies. Yang et al. [32] applied NDEM to investigate the influence of the ice geometry during ice breaking on ship resistance, further confirming the effectiveness and stability of the method in predicting ice resistance.

In summary, the discrete element method (DEM)—and in particular its extended form, the non-smooth discrete element method (NDEM)—offers a promising solution for maneuvering simulations in broken ice environments, balancing detailed contact modelling with computational efficiency. It demonstrates unique advantages in capturing the dynamic behaviours of ships operating in floating ice conditions.

Previous studies on ship-ice interaction have focused primarily on the influence of parameters such as ship speed, ice thickness, and ice concentration on navigational performance, laying a solid theoretical foundation for ship operations in ice-covered regions. However, systematic investigations into ship maneuverability—particularly steering performance and other dynamic operational behaviours—remain relatively limited. Coupling the Maneuvering Modelling Group (MMG) model with ice load models has emerged as both a technical challenge and a research hotspot in recent years. Several studies have attempted

to integrate the MMG maneuvering framework with discrete element-based ice force models to simulate ship behaviour in densely packed ice fields. For example, Zhan et al. [33] developed a simulation system integrating Oceanic Consulting's open water maneuvering code (based on the MMG model) with INTERA's discrete element ice load module, successfully reproducing the turning circle and Zig-Zag manoeuvres of multiple ships in floating ice environments, and analyzing the motion differences between ice-covered and ice-free conditions. Zhou et al. [34] employed a three-degree-of-freedom (3-DOF) maneuvering model and discretized the ice edge and the waterline to predict the resistance to ice and the yaw moments during turning manoeuvres. The predictions were validated using Planar Motion Mechanism (PMM) tests on a 1:20 scale model of an icebreaker of class R. Expanding on this work, Di et al. [35] introduced a DEM-based model that incorporates the interactions of the bonded particles into a six-degree-of-freedom (6-DOF) maneuvering framework. Their model considered the coupling effects of the propeller, rudder, and hydrodynamic forces, and successfully simulated the turning characteristics of the *Xuelong* icebreaker under broken and intact ice conditions. More recently, Yang et al. [36] proposed a simulation framework that binds NDEM to a 3-DOF MMG model, allowing full-scale simulation of ship maneuvering in broken ice environments. Their study systematically assessed the effects of ice concentration, floe size and thickness, ship speed, and rudder angle on maneuvering performance.

Despite progress in ship maneuvering research in ice-covered waters, key limitations remain. A major gap lies in the lack of effective coupling between high-fidelity ice load models and maneuvering dynamics frameworks. Most studies use simplified ice force representations, limiting accuracy under complex ice conditions. Although NDEM has been applied in maneuvering simulations, it has rarely been combined with the MMG model. Such coupling can overcome the small-time-step and efficiency issues of DEM or CFD-DEM in large-scale, high-frequency collisions, while maintaining numerical stability and accuracy. This makes it especially suitable for simulating dynamic ship–ice interactions. However, the maneuvering performance of conventional merchant ships in broken ice remains underexplored, despite growing navigation in marginal ice zones due to climate change. Reliable simulation tools for these vessels are still lacking.

To address this gap, this study conducts high-fidelity numerical simulations to investigate the maneuvering performance of non-icebreaking ships navigating in floating ice regions, taking the benchmark S175 container ship as a representative case. The main contributions of this work are as follows:

- A coupled MMG–NDEM maneuvering simulation framework is developed for the quantitative analysis of ship–ice interactions involving non-icebreaking vessels. This framework integrates the Non-Smooth Discrete Element Method (NDEM) with the three-degree-of-freedom MMG maneuvering model, enabling the simultaneous consideration of hydrodynamic forces and ice–ship contact dynamics within a unified computational environment.
- A comprehensive numerical investigation is carried out to evaluate the maneuvering performance of the S175 container ship, including standard turning circle and Zig-Zag maneuvers, under a range of representative ice conditions.
- A systematic parametric study is performed to quantify the effects of ice floe size, ice concentration, and ice incidence angle on turning capability and steering stability, thereby revealing the underlying physical mechanisms responsible for maneuvering performance degradation in ice-covered waters. The findings not only advance the understanding of non-icebreaking ship behaviour in such environments but also provide scientific support for navigational safety assessments, operational planning, and the development of Arctic shipping routes.

2. Numerical Method

2.1. 3 DOF Maneuvering Model

In this study, two coordinate systems are employed: the Earth-fixed coordinate system and the body-fixed coordinate system. The latter moves with the ship at the maneuvering speed, but does not follow the ship's oscillatory motions. In the body-fixed coordinate system, the x - y plane coincides with the surface of the still water, as illustrated in Figure 1. The positive x axis and the y axis point to the bow and starboard sides of the ship, respectively. The variables u and v denote the surge and sway velocities of the ship, δ denotes the rudder angle, β is the drift angle, and ψ is the heading angle of the ship.

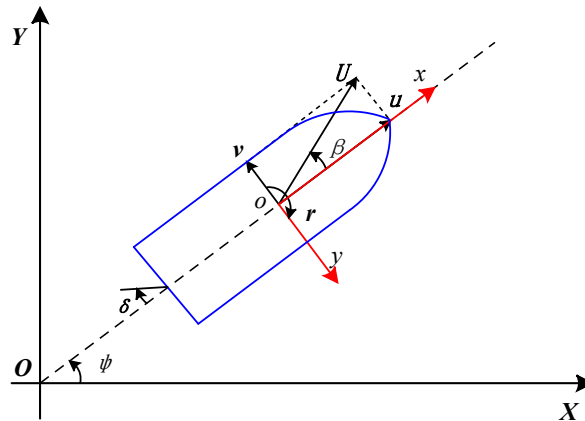


Figure 1. Earth-fixed and body-fixed coordinate systems used for maneuvering modeling.

The relationship between the earth-fixed coordinate system and the body-fixed coordinate system can be expressed as follows.

$$\begin{cases} X = x \cos \psi(t) - y \sin \psi(t) + X_0(t) \\ Y = x \sin \psi(t) + y \cos \psi(t) + Y_0(t) \\ Z = z \end{cases} \quad (1)$$

where $(X_0(t), Y_0(t))$ denotes the position coordinates of the ship in the Earth-fixed coordinate system and t represents time.

The MMG model with three degrees of freedom (3-DOF) is utilized. According to the conceptual framework of the MMG model, the external forces and moments (X, Y, N) that affect the movement of the ship are decomposed into fluid inertia forces, fluid viscous forces, propeller thrust, and rudder forces acting on the hull [37]. The basic structure of the MMG mathematical model is represented as shown in Equation (2).

$$\begin{cases} (m + m_x)\dot{u} - (m + m_y)vr = X_H + X_P + X_R \\ (m + m_y)\dot{v} + (m + m_x)ur = Y_H + Y_R \\ (I_{zz} + J_{zz})\dot{r} = N_H + N_R \end{cases} \quad (2)$$

where m represents the mass of the ship. The terms m_x and m_y represent the added masses along the x axes and the y axes, respectively. J_{zz} represents the added inertia moments on the z axes. The subscripts H , P , and R mean the hydrodynamic forces acting on the hull, propeller, and rudder, respectively.

The hydrodynamic force acting on the hull is expressed as follows.

$$\begin{cases} X_H = 0.5\rho LdV^2 X'_H(v', r') - \mathcal{R}(u_0) \\ Y_H = 0.5\rho LdV^2 Y'_H(v', r') \\ N_H = 0.5\rho L^2 dV^2 N'_H(v', r') \end{cases} \quad (3)$$

with

$$\begin{cases} X'_H(v', r') = X'_{vv}v'^2 + X'_{vr}v'r' + X'_{rr}r'^2 \\ Y'_H(v', r') = Y'_vv' + Y'_vr' + Y'_{vvv}v'^3 + Y'_{vvv}v'^2r' + Y'_{vvr}v'r'^2 + Y'_{rrr}r'^3 \\ N'_H(v', r') = N'_vv' + N'_vr' + N'_{vvv}v'^3 + N'_{vvv}v'^2r' + N'_{vvr}v'r'^2 + N'_{rrr}r'^3 \end{cases} \quad (4)$$

where $\mathcal{R}(u_0)$ represents the resistance coefficient of the ship. The components X_H , Y_H , and N_H correspond to the forces or moments in the surge, sway, and yaw directions, respectively. The total speed is calculated as $V = \sqrt{u^2 + v^2}$. The nondimensional form of r is given by $r' = \frac{rL}{V}$. The coefficients X'_{vv} , Y'_{vr} , N'_{rr} , etc., represent the hydrodynamic derivatives with respect to specific physical variables. These coefficients, which are indicative of the nonlinear hydrodynamic behaviour of the ship, are typically determined through Planar Motion Mechanism (PMM) tests or Circular Motion Tests (CMT). It is important to note that the specific form of the expressions of the hydrodynamic derivatives is not unique. Polynomial forms proposed by Yasukawa et al. [38,39] generally provide more accurate descriptions of the variation in the hydrodynamic coefficients, offering greater reliability for the precise prediction of the characteristics of the movement of the ship.

The rudder force provides the primary moment required for the maneuvering motion of the ship and is expressed as follows.

$$\begin{cases} X_R = -(1 - t_R)F_N \sin \delta \\ Y_R = -(1 + a_H)F_N \cos \delta \\ N_R = -(x_R + a_H x_H)F_N \cos \delta \end{cases} \quad (5)$$

where t_R represents the thrust deduction factor for the rudder and a_H denotes the increase factor in the rudder force. The variables x_R and x_H refer to the longitudinal coordinates of the center of the rudder and the additional lateral force acting point, respectively. F_N represents the normal rudder force [39], which is calculated as:

$$F_N = \frac{1}{2}\rho \frac{6.13\Lambda}{\Lambda + 2.25} A_d U_R^2 \sin \alpha_R \quad (6)$$

where ρ represents the density of water, and Λ and A_d denote the aspect ratio of the rudder and the area of the rudder, respectively. U_R and α_R represent the resultant inflow velocity to the rudder and the effective inflow angle, respectively. The estimation formulas for these parameters are as follows:

$$\begin{cases} \alpha_R = \delta - \tan^{-1} \left(\frac{v_R}{u_R} \right) \\ u_R = u_p \varepsilon \sqrt{1 + 8kK_T / (\pi J_P^2)} \\ u_p = u \left[(1 - w_p) + \tau \beta_P^2 \right] \\ v_R = \left(\gamma v' + C_{Rr}r' + C_{Rrrr}r'^3 + C_{Rrrv}r'^2 v' \right) U \\ U_R^2 = u_R^2 + v_R^2 \end{cases} \quad (7)$$

where ε , k , τ , and γ represent the interaction coefficients between the hull, propeller, and rudder. The term v_R denotes the inflow velocity in the direction x in the rudder, while

C_{Rr} , C_{Rrrr} , and C_{Rrrv} are experimental constants that accurately describe v_R [40]. The variables u_p and v_R refer to the inflow velocities in the propeller and rudder, respectively. Furthermore, K_T , w_p , and J_P correspond to the propeller thrust coefficient, wake coefficient, and propeller advance ratio, respectively.

The lateral forces and yaw moments generated by the propeller are typically minimal and difficult to measure. In the MMG model, these effects are typically considered in combination with the hydrodynamic maneuvering forces acting on the hull, so only the longitudinal hydrodynamic forces generated by the propeller require calculation.

The hydrodynamic forces generated by the propeller can be expressed as

$$X_P = (1 - t_p) \rho n_p^2 D_p^4 K_T(J_P) \quad (8)$$

$$K_T(J_P) = j_0 + j_1 J_P + j_2 J_P^2 \quad (9)$$

$$J_P = \frac{u(1 - w_p)}{n D_P} \quad (10)$$

where t_p and n_p represent the thrust reduction coefficient and the propeller revolution, respectively. D_p denotes the diameter of the propeller, while K_T represents the propeller thrust coefficient. K_T can be expressed as a quadratic polynomial in terms of J_p , where J_p is the advance coefficient, and w_p is the wake coefficient; J_0 , J_1 , and J_2 are regression parameters. More details of the maneuvering coefficients related to the propeller, the rudder, and the hull forces can be found in [41,42].

It is worth noting that the present study adopts a three-degree-of-freedom (3-DOF) maneuvering model, incorporating surge (u), sway (v), and yaw (r) motions. This simplification follows the classical MMG framework and is based on the assumption that, under most floating ice conditions, ice loads act predominantly near the waterline and primarily induce motions in the horizontal plane. The 3-DOF formulation also enables more efficient computations, facilitating extensive parametric investigations. However, in certain situations, such as concentrated bow impacts or heavy ice conditions, vertical-plane responses, including pitch and heave, as well as roll motions, may become non-negligible due to the distribution and magnitude of ice–ship contact forces. The present model does not explicitly account for such six-degree-of-freedom coupling effects, and therefore its applicability is most appropriate for moderate speed of ships and ice concentrations of approximately 20–60%. This limitation is further discussed in the Conclusion, where potential extensions to a full 6-DOF framework are outlined.

2.2. Ice Resistance Model

During navigation in broken ice regions, the hull of the ship frequently experiences collisions and frictional interactions with floating ice. Discrete ice floes introduce additional resistance and moments on the hull surface, significantly affecting ship maneuvering performance. In this study, the ship–ice interaction is modelled as a discontinuous contact process between multiple rigid ice floes and the ship hull. Each ice floe is simplified as a two-dimensional rigid body with defined mass, velocity, and moment of inertia, possessing independent translational and rotational degrees of freedom. This modelling assumption is a commonly adopted and effective simplification in studies of ship–ice interaction, providing a reasonable representation of the dynamic behaviour of floating ice during collision processes.

2.2.1. Collision Detection Method

In numerical simulations of ship–ice interactions, it is essential to resolve two primary types of collisions: those between the ship hull and ice floes, and those among ice

floes themselves. The efficiency of the collision detection stage largely determines the overall computational performance of the simulation framework. To address this, a two-stage hybrid strategy is adopted, combining the Sweep and Prune (SAP) algorithm for broad-phase filtering and the Gilbert–Johnson–Keerthi (GJK) algorithm for narrow-phase contact resolution.

In the broad-phase, SAP rapidly excludes distant objects that cannot physically interact by constructing axis-aligned bounding boxes (AABBs) for each object, projecting them onto coordinate axes, and sorting the boundary coordinates. Overlaps are identified by traversing the sorted lists, reducing the number of potential collision pairs from $O(n^2)$ to near-linear complexity under sparse contact conditions (Figure 2). The remaining candidate pairs are passed to the GJK algorithm, which determines whether two convex bodies intersect by analyzing the Minkowski difference between them. If the origin lies within this difference, a collision is detected. GJK iteratively constructs a simplex toward the origin using support functions, providing not only the intersection status but also the minimum distance vector and penetration depth. Its geometric robustness and efficiency make it well-suited for frequent, high-precision contact checks in rigid-body simulations.

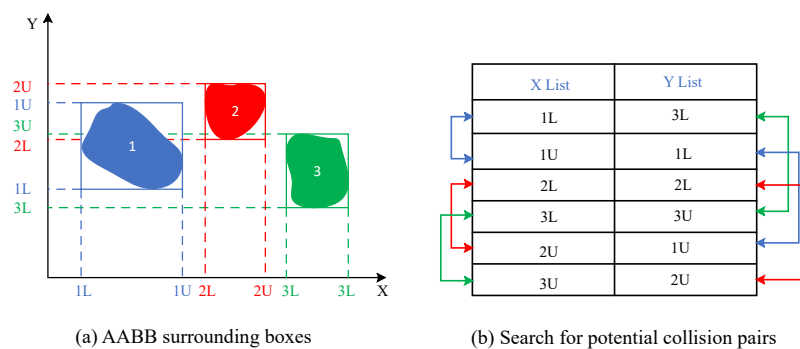


Figure 2. SAP algorithm diagram. (a) Axis-aligned bounding boxes (AABB) of three objects. (b) Search process for potential collision pairs. Blue, red, and green represent different objects.

While intelligent collision detection methods based on fuzzy logic and neural networks [43,44] have shown potential in pattern recognition and autonomous navigation, they require substantial labeled data and extensive training, and may lack deterministic guarantees. In contrast, the SAP–GJK combination is data-independent, interpretable, and fully compliant with Newtonian mechanics, making it particularly suitable for high-frequency multibody contact simulations in the NDEM–MMG framework.

2.2.2. Constraint Solving

Once contact bodies and contact point information are obtained, the contact force and normal penetration distance can be treated as complementary variables. A schematic illustration of the collision between body A and body B at the contact point is shown in Figure 3. The collision impulse is calculated based on the change in relative velocity at the contact point before and after impact, following the impulse–momentum relationship for rigid bodies in the Non-Smooth Discrete Element Method (NDEM) [45]. This approach decomposes the total contact impulse into normal and tangential components, where the normal component is associated with the contact normal direction, and the tangential component corresponds to the tangential direction. Both components incorporate the effects of translational and rotational inertia of the colliding bodies, as well as the moment arms from the centers of mass to the contact point. The discrete forms in Equations (11) and (12) are obtained by inverting the effective mass matrix in the local contact frame, ensuring that

the calculated impulses satisfy the non-penetration constraint in the normal direction and the frictional constraint in the tangential direction.

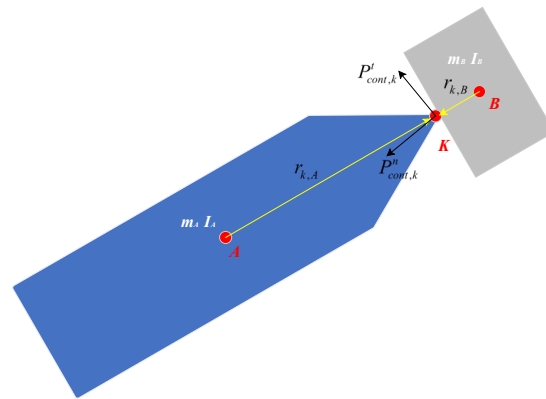


Figure 3. Illustration of the collision between object A and B.

$$\mathbf{P}_{\text{cont},k} = \mathbf{P}_{\text{cont},k}^n + \mathbf{P}_{\text{cont},k}^t \quad (11)$$

$$\begin{cases} \mathbf{P}_{\text{cont},k}^n = \frac{(\Delta \mathbf{V}_{\text{rel}} \times \mathbf{n}) \times \mathbf{n}}{\frac{1}{m_A} + \frac{1}{m_B} + \left[\left(\frac{\mathbf{r}_{k,A} \times \mathbf{n}}{I_A} \right) \times \mathbf{r}_{k,A} \right] \times \mathbf{n} + \left[\left(\frac{\mathbf{r}_{k,B} \times \mathbf{n}}{I_B} \right) \times \mathbf{r}_{k,B} \right] \times \mathbf{n}} \\ \mathbf{P}_{\text{cont},k}^t = \frac{(\Delta \mathbf{V}_{\text{rel}} \times \mathbf{t}) \times \mathbf{t}}{\frac{1}{m_A} + \frac{1}{m_B} + \left[\left(\frac{\mathbf{r}_{k,A} \times \mathbf{t}}{I_A} \right) \times \mathbf{r}_{k,A} \right] \times \mathbf{t} + \left[\left(\frac{\mathbf{r}_{k,B} \times \mathbf{t}}{I_B} \right) \times \mathbf{r}_{k,B} \right] \times \mathbf{t}} \end{cases} \quad (12)$$

where $\mathbf{P}_{\text{cont},k}^n$ and $\mathbf{P}_{\text{cont},k}^t$ denote the normal and tangential collision impulses, respectively; m_A and m_B represent the masses of the collision bodies A and B; $\Delta \mathbf{V}_{\text{rel}}$ is the change in relative velocity at the contact point k ; and $\mathbf{r}_{k,A}$ and $\mathbf{r}_{k,B}$ are the position vectors from the center of mass of bodies A and B to the contact point. I_A and I_B denote the inertia tensors of bodies A and B, respectively; \mathbf{n} and \mathbf{t} represent the normal and tangential unit vectors. In addition, the tangential collision impulse must satisfy the Coulomb friction law, which is expressed as Equation (13):

$$-\mu \left\| \mathbf{P}_{\text{cont},k}^n \right\| \leq \mathbf{P}_{\text{cont},k}^t \leq \mu \left\| \mathbf{P}_{\text{cont},k}^n \right\| \quad (13)$$

where μ is the friction coefficient.

It should be noted that impulse-based response models grounded in non-smooth dynamics theory do not directly compute contact forces. In this study, the contact force is estimated using the contact force conversion model proposed by Yulmetov et al. [46], which classifies contact events into collision contact or static contact. For static contact, the contact force is approximated based on the variation of the impulse during the simulation time step. For collision contact, the contact force is calculated using the collision duration T_{col} , which is determined by Equation (14):

$$T_{\text{col}} \approx \frac{\pi}{2} \sqrt{\frac{M^*}{K}} \quad (14)$$

where M^* is the reduced mass and K is the contact stiffness. Given that the mass of floating ice is relatively small compared to the mass of the ship, the reduced mass during ship–ice collisions can be approximated as the mass of the ice. When the ice approaches the hull, the effects of added mass become significant; hence, an added mass coefficient of 1.0 is introduced to estimate the reduced mass, as expressed in Equation (15).

$$M^* \approx (1 + \alpha)M_{\text{ice}} \quad (15)$$

where α is the added mass coefficient and M_{ice} is the mass of the interacting ice floe. Contact stiffness K is a key parameter commonly used in Discrete Element Method (DEM) modelling. In the present study, a contact stiffness of 1.0×10^6 N/m is selected for the numerical simulations [47]. It is worth noting that the calculation of the duration of the collision here considers only the effect of body mass on the collision process and does not account for the influence of simultaneous multibody contact or eccentric collisions.

2.3. Ice Field Generation

In this study, the numerical ice field is made up of identical rectangular ice floes. Therefore, the generation of the ice field requires only the initialization of the floe positions and orientations. The coordinates of each floe vertex in the ice field are calculated using Equation (16) [48]:

$$\begin{cases} P'_{i,x} = P_{i,x} \cos \alpha - P_{i,y} \sin \alpha + P_{\text{loc},x} \\ P'_{i,y} = P_{i,x} \sin \alpha + P_{i,y} \cos \alpha + P_{\text{loc},y} \end{cases} \quad (16)$$

where $(P_{i,x}, P_{i,y})$ are the original vertex coordinates of the ice floe, α is a randomly assigned rotation angle, and $(P_{\text{loc},x}, P_{\text{loc},y})$ are the initialized centroid coordinates of the floe. The final floe vertex coordinates $(P'_{i,x}, P'_{i,y})$ are obtained through random rotation and translation, as illustrated in Figure 4. During the ice field generation process, the SAP and GJK algorithms are also used to perform preliminary screening and fine-level validation to ensure that the ice floes do not overlap.

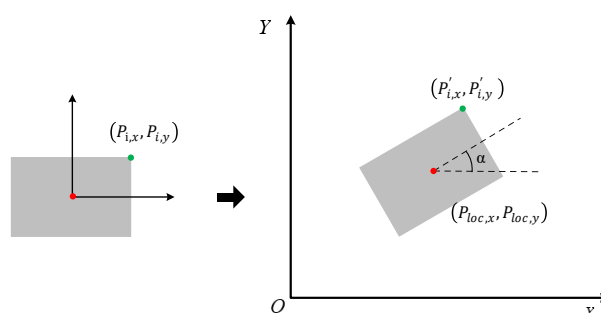


Figure 4. Determine the random distribution of ice floes.

2.4. Fluid Force Model

The motion of broken ice in water is influenced by buoyancy forces and hydrodynamic drag. In this study, the hydrodynamic forces that act on the ice floes are modelled using the Morison equation, as expressed in Equation (17):

$$\begin{cases} \mathbf{F}_{\text{drag}} = -0.5 C_d \rho_w A_{\text{proj}} \mathbf{U}_{\text{rel}} |\mathbf{U}_{\text{rel}}| \\ \boldsymbol{\tau}_{\text{drag}} = -0.5 C_a \rho_w l_{\text{avg}}^3 A_{\text{sub}} \boldsymbol{\Omega} |\boldsymbol{\Omega}| \end{cases} \quad (17)$$

where C_d and C_a are the drag coefficient and the rotational damping coefficient, respectively; ρ_w is the water density; A_{proj} and A_{sub} denote the projected area and submerged area of the ice floe; and \mathbf{U}_{rel} and $\boldsymbol{\Omega}$ represent the relative translational velocity and the angular velocity, respectively. This model effectively captures the hydrodynamic response of ice floes under fluid forces.

2.5. Ship–Ice Coupled Model

To simulate ship maneuvering behaviour in floating ice regions, this study establishes a dynamic simulation framework that couples a three-degree-of-freedom (3-DOF) ship maneuvering model (MMG) with the Non-Smooth Discrete Element Method (NDEM). The general flow diagram of numerical simulation is illustrated in Figure 5. Within this framework, the ship is subjected to hydrodynamic forces generated by the propeller and rudder, while simultaneously undergoing multiple-point collisions with ice floes. These collisions induce discontinuous impulsive forces and moments, which significantly affect the performance of the maneuvering of the ship. To complement the schematic in Figure 5, the algorithmic sequence of the coupled MMG–NDEM simulation is summarized in Algorithm 1. This pseudocode outlines the core steps taken in each simulation time step, including ship dynamics update, contact detection and response, and integration.

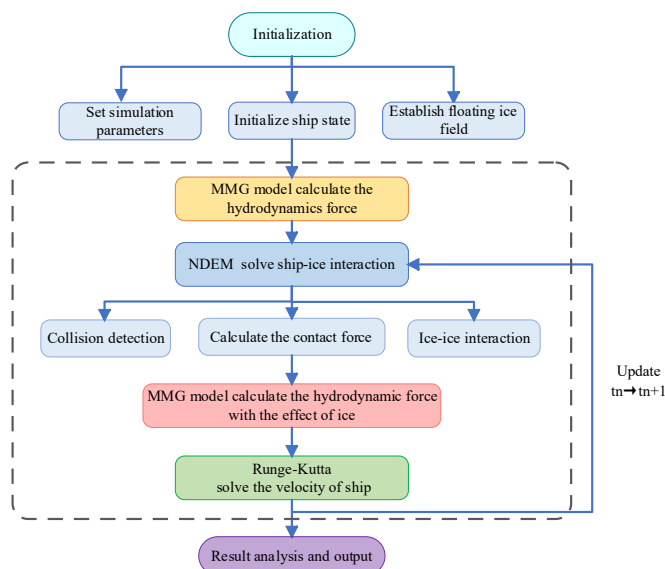


Figure 5. Coupled MMG-NDEM scheme for ship maneuvering simulation in broken ice area.

Algorithm 1: Coupled MMG–NDEM simulation loop

Input: Simulation parameters, initial ship state, initial ice field

Output: Time evolution of ship motion and ice responses

Initialization:

Set time step Δt , total duration T , and initialize $t \leftarrow 0$

Initialize ship position and velocity from MMG model

Generate floating ice field with randomized floe positions and orientations

while $t < T$ **do**

 Compute hydrodynamic forces on ship from MMG model;

 Predict rigid body motion of ship using MMG equations;

 /* Broad-phase collision detection */

 Apply SAP algorithm to identify potential contact pairs (ship-ice and ice-ice);

 /* Narrow-phase collision detection */

 Use GJK algorithm to test each pair and obtain contact points and normals;

 Compute contact forces and impulses via NDEM solver;

 Update ship velocity and angular rate using Runge–Kutta integration;

 Update ice floe positions and orientations;

$t \leftarrow t + \Delta t$;

return Final ship trajectory and ice distribution

In the subsequent coupling process, the MMG model provides the velocity and position parameters of the ship required by the NDEM model to calculate ship–ice interactions. After updating the position and velocity of the ship, the NDEM collision solver is used to calculate the ice forces acting on the hull. The computed ice forces are then fed back into the MMG model. The governing equations follow the standard 3-DOF MMG maneuvering model [37], which describes the ship’s horizontal-plane dynamics. In this study, the model is extended by introducing additional force terms— X_{ice} , Y_{ice} , and N_{ice} —to account for ice loads computed by the NDEM model. The resulting coupled equations are expressed as Equation (18):

$$\begin{cases} (m + m_x)\dot{u} - (m + m_y)vr = X_H + X_P + X_R + X_{ice} \\ (m + m_y)\dot{v} + (m + m_x)ur = Y_H + Y_R + Y_{ice} \\ (I_{zz} + J_{zz})\dot{r} = N_H + N_R + N_{ice} \end{cases} \quad (18)$$

The MMG model computes maneuvering forces and hydrodynamic responses based on the current motion state of the ship, which are then used to determine the acceleration and dynamic behaviour of the ship. To ensure high accuracy and numerical stability, the fourth-order Runge–Kutta method (RK4) is employed to solve the integral Equation (18).

Since the ice forces are calculated in the earth-fixed coordinate system, they must be transformed into the body-fixed coordinate system. The transformation is given by Equation (19):

$$\begin{cases} X_{ice} = F_{ice,x} \cos \psi + F_{ice,y} \sin \psi \\ Y_{ice} = -F_{ice,x} \sin \psi + F_{ice,y} \cos \psi \\ N_{ice} = M_{ice,z} \end{cases} \quad (19)$$

where ψ is the angle of direction of the ship. The transformed forces X_{ice} , Y_{ice} and the moment N_{ice} , together with the propeller thrust and the rudder forces, are input into the 3-DOF MMG equations to update the velocity of the ship and the angular velocity.

3. Results and Discussion

3.1. MMG Model Validation in Open Water

Due to the lack of experimental data available on the turning performance of ships in fractured ice regions for comparative analysis, this study performs independent validation of the NDEM and MMG models. Previous research [32] has validated the numerical simulation results of ship–ice collision processes, providing methodological reference and theoretical support for the present study. In this study, the S175 container ship, a classical benchmark vessel widely used in maneuvering research and validated through extensive model tests and CFD simulations, was selected as a representative non-icebreaking merchant ship for hydrodynamic investigations. Figure 6 illustrates the three-dimensional hull form of the S175 model used in this study, which forms the basis for subsequent numerical simulations. Numerical simulations of turning circle and Zig-Zag maneuvers were performed under open-water conditions using the proposed MMG model, and the results were compared against available experimental data to validate its effectiveness. The principal dimensions and hull form coefficients of the S175 container ship are listed in Table 1. Furthermore, the relative coefficients used in the MMG model, which characterize the hydrodynamic contributions of the hull, propeller, and rudder to surge, sway, and yaw motions, are summarized in Table 2 [40].

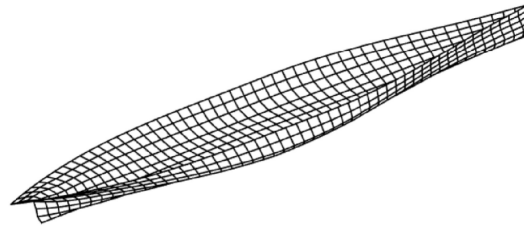


Figure 6. Three-dimensional geometry of the S175 container ship model used in this study. The data were from [49].

Table 1. Principal dimensions and parameters of the S175 container ship and its scaled model.

Category	Parameter	Full Scale	Model Scale
Hull	Length between perpendiculars, L (m)	175.0	3.0337
	Beam, B (m)	25.4	0.4403
	Draft, D (m)	9.5	0.1647
	Displacement, ∇ (m ³)	24742	0.127
	Coordinate of center of gravity	(−2.545, 0, 0)	(−0.042, 0, −0.01)
	Metacentric height	—	0.0173
	Radius of gyration in roll, k_{xx}	0.33 B	0.33 B
	Radius of gyration in pitch, k_{yy}	0.25 L	0.25 L
	Radius of gyration in yaw, k_{zz}	0.269 L	0.269 L
	Wetted surface area (m ²)	5396	1.6216
Propeller	Diameter, D_p (m)	6.5064	0.1128
	Pitch ratio	0.915	0.915
	Number of blades	5	5
Rudder	Area, A_d (m ²)	32.46	0.0098
	Height, H (m)	7.7	0.1335
	Aspect ratio, Λ	1.8268	1.8268

Table 2. Hydrodynamic derivatives and interaction coefficients for the 3-DOF MMG maneuvering model of the S175 container ship.

	Symbol	Value	Symbol	Value	Symbol	Value
Hull	m'_x	0.000238	Y'_v	−0.0116	N'_v	−0.00385
	m'_y	0.007049	Y'_r	0.00242	N'_r	−0.00222
	J'_{xx}	0.0000034	Y'_{vvv}	−0.109	N'_{vvv}	0.001492
	J'_{zz}	0.000419	Y'_{vvr}	0.0214	N'_{vvr}	−0.0424
	X'_{vv}	−0.00386	Y'_{vrr}	−0.0405	N'_{vrr}	0.00156
	X'_{vr}	−0.00311	Y'_{rrr}	0.00177	N'_{rrr}	−0.00229
	X'_{rr}	0.0002	Z_H/D	0.5	N_{10}	0.0082
	C_r	0.001	k_f	1.04		
Propeller	t_p	0.175	$1-w_{p0}$	0.816	x_p	−0.47
	j_0	0.5179	j_1	−0.1179	j_2	−0.3618
Rudder	t_R	0.29	x'_H	−0.48	x'_R	−0.5
	a_H	0.237	ε	0.921	γ	0.088 ($v' < 0$)
	K	0.631	Z_H/D	0.7	γ	0.193 ($v' \geq 0$)
	C_{Rr}	−0.156	C_{Rrr}	−0.275	C_{Rrvv}	1.96

First, the numerical simulation results of the S175 container ship model are compared with the experimental turning trajectory, as shown in Figure 7. The experimental data were obtained from tests conducted in the Ocean Engineering Basin of Shanghai Jiao Tong University (50 m × 30 m × 5 m), using a ship model with a scale ratio of 1:57.689.

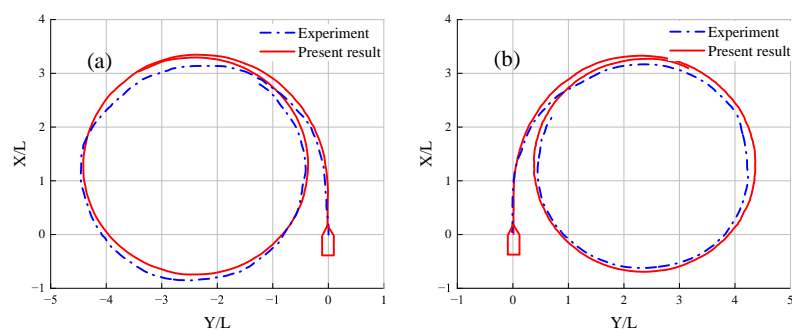


Figure 7. S175 container ship model turning trajectories: (a) port turning ($\delta = -35^\circ$); (b) starboard turning ($\delta = 35^\circ$).

By comparing the diameter of the turn and the advance, the errors of the port and starboard turning diameters were found to be 3% and 5%, respectively, while the errors of the port and starboard advances were both approximately 9%. The comparison results are summarized in Table 3. These results demonstrate that the MMG model can effectively simulate the turning motion of the ship.

Table 3. Relative errors of turning diameter and advance for port and starboard turning.

Turning Diameter	Relative Error	Advance	Relative Error
Port turning	3%	Port turning	9%
Starboard turning	5%	Starboard turning	9%

In addition, a comparative analysis was conducted between the simulated response to the heading angle of the S175 container ship during the Zig-Zag maneuver and the corresponding experimental data, as shown in Figure 8. The first and second overshoot angles computed in the numerical simulation agree well with the experimental results reported by [50]. This further validates the accuracy and reliability of the 3-DOF MMG model proposed in this study.

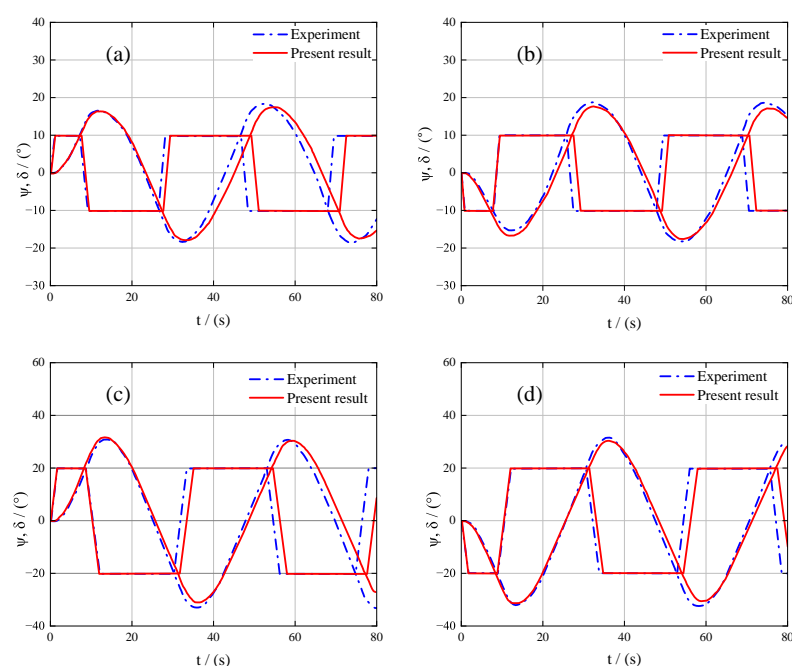


Figure 8. S175 container ship model Zig-Zag maneuver: heading and rudder angle time history curves in calm water—(a) $10^\circ/10^\circ$ (starboard rudder); (b) $-10^\circ/-10^\circ$ (port rudder); (c) $20^\circ/0^\circ$ (starboard rudder); (d) $-20^\circ/-20^\circ$ (port rudder).

3.2. Turning Maneuver of the Ship in Broken Ice Fields

3.2.1. Effect of Ice Concentration

Ice concentration is a key parameter for quantifying the extent of ice coverage, typically used to describe the proportion of a given water area that is covered by ice floes. In this study, following the WMO sea ice classification standards and recommended navigability guidelines for non-icebreaking ships, three typical ice fields with concentrations of 20%, 40%, and 60% were selected for simulation. Each ice field consists of rectangular ice floes with dimensions of $0.25\text{ m} \times 0.20\text{ m} \times 0.02\text{ m}$, covering a total area of $20\text{ m} \times 20\text{ m}$. The three ice fields with different concentrations are illustrated in Figure 9.

A concentration of 20% represents a sparse ice region where non-icebreaking ships can navigate relatively freely, while concentrations of 40% to 60% represent typical medium-concentration broken ice fields, which are commonly encountered by such ships during navigation. When the ice concentration exceeds 70%, non-icebreaker ships generally cannot navigate independently; therefore, this condition was not considered in the present study. The simulation parameters are summarized in Table 4.

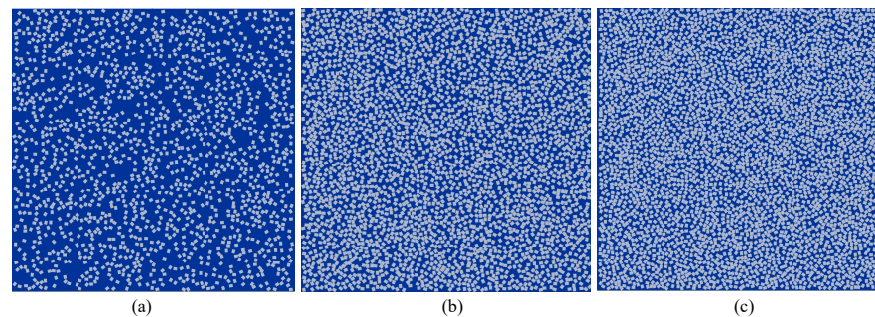


Figure 9. Floating ice fields with different ice concentrations: (a) 20%; (b) 40%; (c) 60%.

Table 4. Physical and numerical parameters used in the simulations.

Parameter	Value
Water density (kg/m^3)	1025
Ice density (kg/m^3)	917
Ship–ice friction coefficient	0.28
Ship–ice restitution coefficient	0.50
Ice–ice friction coefficient	0.44
Ice–ice restitution coefficient	0.25
Time step (s)	0.002
Form drag coefficient, C_d	1.0
Angular drag coefficient, C_a	0.05

Figure 10 presents the turning trajectories of the S175 container ship in floating ice fields with different ice concentrations (20%, 40%, and 60%). The corresponding numerical simulation results are summarized in Table 5. It can be clearly observed that as the ice concentration increases, the overall turning trajectory of the ship is more contracted and the turning diameter is significantly reduced. This indicates that floating ice has a considerable impact on the turning ability of the ship. However, this does not imply an improvement in maneuvering performance, as the time required for the ship to complete the same turning angle increases in high-concentration ice regions. In open water, the ship moves freely along its inertial path under the dominance of hydrodynamic forces, resulting in the largest turning radius. As the concentration of ice increases to 20% and 40%, the presence of floating ice introduces disturbances to the motion of the ship. In particular, an outer “barrier” effect emerges along the outer turning path, constraining the lateral motion of

the ship and thus limiting the outward side slip, causing the turning trajectory to contract inward. In medium density (40%) and higher ice fields, frequent contact between the outer hull and stern of the ship with floating ice produces a passive constraint effect, leading to further contraction of the trajectory boundaries. These results demonstrate that ship maneuverability is substantially inhibited in high concentration floating ice regions, a trend that is consistent with findings from previous studies on ship maneuver performance in ice-covered waters [33,36].

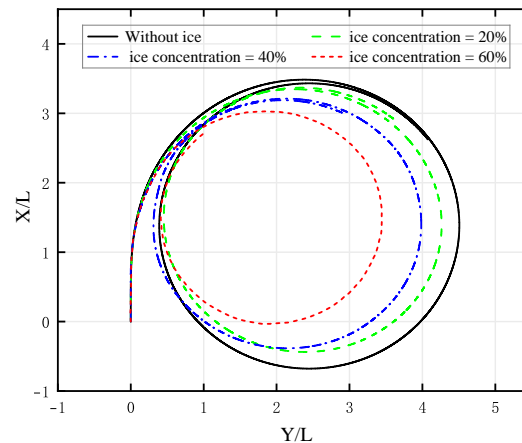


Figure 10. Turning trajectories of the S175 container ship under different ice concentrations: 20%; 40%; and 60%.

Table 5. Simulated turning performance of the S175 container ship under different ice concentrations.

Ice Concentration (%)	Tactical Diameter D_T (m)	Time to 180° Turning (s)	Turning Diameter D (m)	Steady Speed (m/s)	Angular Velocity (rad/s)
0	4.51L	35.27	4.11L	0.549	0.090
20	4.31L	35.98	3.81L	0.524	0.089
40	3.99L	37.12	3.78L	0.457	0.085
60	3.40L	38.16	3.21L	0.258	0.080

L is the ship length between perpendiculars.

According to the classical geometric relationship of turning motion, the turning diameter of a ship is determined by its forward velocity V and angular velocity r as expressed in Equation (20):

$$D = \frac{2V}{r} \quad (20)$$

Based on this, if the motion states of the ship in open water and in regions covered by ice are indicated as (V_0, r_0) and (V_1, r_1) , respectively, the turning radius will increase when the following condition is met:

$$\frac{V_1}{r_1} > \frac{V_0}{r_0} \quad (21)$$

In addition to incorporating the effects of ice forces, changes in forward velocity and angular velocity under ice disturbance can be expressed as

$$\begin{cases} \Delta V = \left(\frac{F_{ice}}{m} + a_{v1} - a_{v0} \right) \Delta t \\ \Delta r = \left(\frac{T_{ice}}{I} - a_{r1} + a_{r0} \right) \Delta t \end{cases} \quad (22)$$

where ΔV and Δr represent the reductions in velocity and angular velocity caused by the combined effects of ice forces and hydrodynamic forces, while F_{ice} and T_{ice} denote the resistance to ice in direction and the ice-induced moment, respectively.

The simulation results indicate that as the ice concentration increases, the stable turning speed of the ship decreases from 0.549 m/s to 0.258 m/s—an over 50% reduction—whereas the angular velocity decreases from 0.090 rad/s to 0.080 rad/s, with a relatively smaller reduction. This suggests that in floating ice environments, the reduction in forward velocity is much greater than the reduction in angular velocity, meaning that the ship can maintain a certain turning tendency despite. According to Equation (20), when the reduction in angular velocity is less than the forward velocity, the turning radius will decrease, which is consistent with the results of the numerical simulation. According to the ice-induced disturbance criterion proposed by Yang et al. [36], the turning radius will increase when the inhibitory effect of ice moments on angular velocity exceeds the decelerating effect of ice resistance on forward velocity; otherwise, the turning radius will decrease. In this study, under 40% ice concentration, the reduction in angular velocity is less than that of forward velocity, consistent with the observed trajectory contraction. This indicates that in medium-concentration ice conditions, ice resistance dominates the turning characteristics of the ship, and maneuvering strategies should focus on enhancing propulsion efficiency and controlling side-slip motion.

The ship turning trajectory and the local ice interaction process in a field of 40% ice concentration are illustrated in Figure 11. As shown in Figure 11, the ship forms a continuous curved path through the floating ice field during the turning maneuver, indicating significant hull–ice interaction and accumulation along the outer turning edge. Figure 11 presents a magnified view of the local region of contact between the ship and the ice, where multiple discrete ice floes collide with the hull. These collisions generate concentrated resistance and ice moments, particularly around the bow and port-side area, and are responsible for the constrained lateral motion and reduced turning diameter observed in the simulations.

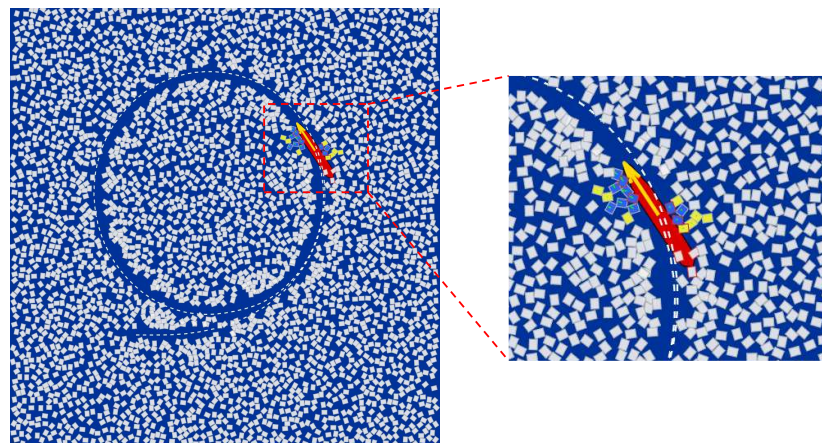


Figure 11. Simulated turning trajectory of the ship in a broken ice field with 40% ice concentration. The left panel shows the global maneuvering path; the right panel presents a magnified view of the local ship–ice interaction region. The yellow arrows indicate the ship’s motion direction, and the red color represents the ship’s hull.

To further elucidate the physical mechanisms underlying the contraction of the turning trajectory of the ship, the time histories of the dimensionless ice resistance and ice moment experienced by the ship during the turning maneuver in a field of ice concentration 40% are presented in Figure 12. As shown in Figure 12a, the ship experiences significant fluctuations in ice resistance during the initial phase of the turning maneuver, mainly due

to large-scale unstable contacts between the bow and the outer hull with floating ice. As the ship gradually transitions into a steady motion state, these fluctuations in ice resistance diminish. This trend indicates that the resistance to ice is predominantly concentrated during the initial phase of the maneuvering process and is a key factor that contributes to the reduction in the turn speed and the contraction of the turning trajectory. Figure 12b depicts the corresponding time history of the dimensionless ice moment. Throughout the maneuver, the ship is predominantly subjected to a negative ice moment, corresponding to a clockwise acting direction. In the initial phase, this negative moment exhibits pronounced fluctuations, indicating that the ship encounters strong interfering thrusts from ice floes on the outer side, which inhibit the growth of angular velocity and directly affect the turning capability of the ship. As the ship completes its adjustment to the direction and gradually overcomes the ice-induced disturbances, the fluctuations in the ice moment decrease significantly and stabilize. These results suggest that the constraining effect of floating ice on the angular velocity of the ship tends to become sustained and stable in the later stages of the turning maneuver, highlighting the directional and persistent characteristics of the passive attitude disturbances induced by the ice field.

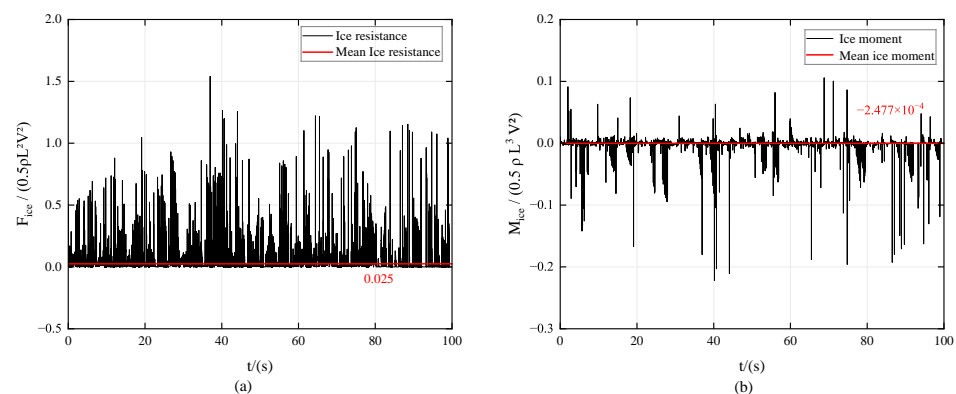


Figure 12. Time histories of the dimensionless ice resistance (a) and ice moment (b) during the turning maneuver of the ship in a 40% ice concentration field.

In summary, floating ice environments exert significant mechanical interference on the turning motion of non-icebreaking ships, which manifests itself in several key aspects. Firstly, outer ice floes create a boundary-limiting effect, leading to a contraction of the ship's turning trajectory. Secondly, substantial ice resistance and negative ice moments during the initial phase of the ship's motion reduce both the forward speed and angular velocity, thus delaying the transition to a stable turning state. Third, in high-concentration ice fields, the increased frequency of ship-s-ice contacts amplifies the disturbance effects, substantially increasing the complexity of the maneuvering process. Therefore, in the planning of navigation paths and the design of maneuvering strategies for non-icebreaking ships operating in ice-covered regions, it is essential to fully account for the combined influences of ice concentration and ice floe distribution to ensure navigational safety and controllability.

3.2.2. Effect of Ice Size

Existing studies on the prediction of ice resistance have consistently shown that the size of the ice floe has a significant impact on both the magnitude and fluctuation of ice resistance. This influence is particularly critical when considering the maneuvering performance of non-icebreaking ships, as excessively large ice floes can severely affect the ship's speed and attitude changes. To verify the rigid-body assumption for the selected floe sizes, we adopt the flexural characteristic length from thin-plate theory on an elastic foundation as a conservative upper bound [51–53]. Sea ice can also fail by crushing, splitting, or mixed

modes depending on confinement and contact conditions; here, the flexural limit is used solely to bound the floe size so that the pre-broken floes in this study are expected to behave as rigid bodies during contact. Cases in which intra-floe deformation or crushing dominates are beyond the scope of the present model. The maximum characteristic size is therefore estimated as:

$$l = \sqrt[4]{\frac{D}{k}} = \sqrt[4]{\frac{Eh^3}{12(1-\nu^2)\rho_w g}} \quad (23)$$

where D is the stiffness of the ice plate, E is the elastic modulus of the water foundation, h is the thickness of the ice, ν is the Poisson ratio, ρ_w is the density of the water, g is the gravitational acceleration. The ice thickness is set to 0.02 m in the model scale, which corresponds to a full-scale thickness of 1.15 m. E and ν are taken as 5 GPa and 0.3, respectively. According to Equation (23), the maximum characteristic size l is calculated to be 16.22 m, corresponding to a model scale size of 0.28 m. Consequently, three representative ice floe sizes are selected in this study: 0.15×0.10 m, 0.20×0.15 m, and 0.25×0.20 m. The ice concentration is fixed at 40%. The three ice fields with different floe sizes are shown in Figure 13.

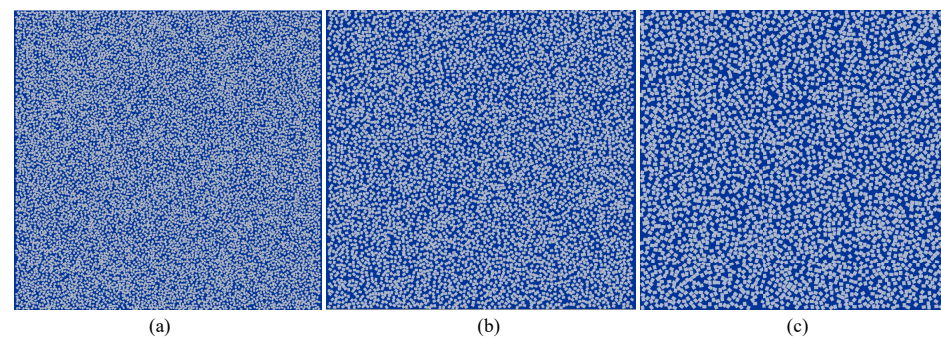


Figure 13. Ice fields with different floe sizes under a fixed ice concentration (40%). The selected floe sizes are (a) 0.15×0.10 m; (b) 0.20×0.15 m; and (c) 0.25×0.20 m.

The results shown in Figure 14 and Table 6 indicate that, under the condition of constant ice concentration, the size of the ice floe has a significant impact on the turning trajectory of the ship and the maneuvering performance. As the size of the ice floe increases, the wing of the ship noticeably contracts inwards, and the diameter of the wing gradually decreases. Small ice floes impose relatively weaker constraints on the motion of the ship, allowing the ship to maintain a higher speed, which results in a larger turning diameter. In contrast, large ice floes exert stronger decelerating and lateral constraint effects on the ship, leading to a noticeably shortened turning path.

This phenomenon can also be explained by the differences in force chain structures formed within the ice field. As illustrated in Figure 15, during ship–ice interactions, large ice floes tend to form stable and longer force chains. These stable force chains are predominantly distributed around the bow and outer regions of the ship, continuously imposing substantial resistance and lateral constraint on the hull. In contrast, although small ice floes interact with the ship at a higher contact frequency and form a greater number of force chains, the chains formed by these smaller ice floes are limited in length, stability, and duration and therefore cannot exert a sustained blocking effect. Instead, they mainly produce random and frequent disturbance effects. As a result, in ice fields with small floes, the ship experiences weaker lateral constraints and maintains a higher speed, leading to a larger turning radius. In contrast, in fields with large floes, the lateral constraints and decelerating effects are significantly enhanced, resulting in a markedly reduced turning radius.

From the perspective of the evolution of the velocity of the ship and the angular velocity, the influence of the size of the ice floe on the maneuver performance also exhibits significant differences. The force chains formed in the bow region primarily contribute to longitudinal deceleration, while those formed along the side of the ship directly affect variations in angular velocity. In small ice floe regions, frequent side contacts generate short and unstable force chains that tend to induce high-frequency disturbances in angular velocity, thereby reducing the stability of the turning motion and resulting in a larger overall turning radius. In contrast, in large ice floe regions, stable and persistent force chains not only enhance the longitudinal deceleration effect, but also effectively suppress fluctuations in angular velocity, leading to a noticeably contracted turning trajectory. In general, large ice floes dominate the characteristics of the turning motion by increasing resistance and lateral constraints, while in small ice floe regions, the ship exhibits greater dynamic freedom and a larger turning radius.

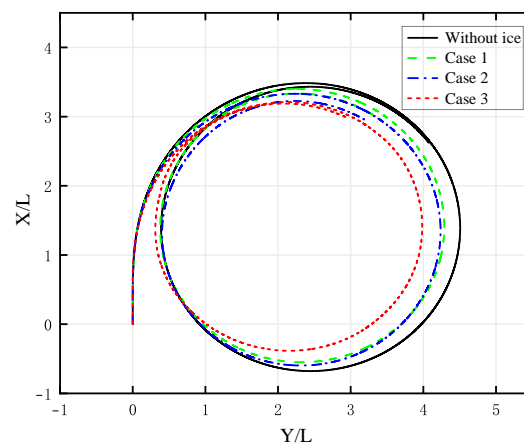


Figure 14. Comparison of ship turning trajectories under different ice floe sizes at a fixed ice concentration of 40%. The solid black line indicates the trajectory in open water (without ice), while Cases 1–3 correspond to floe sizes of (a) 0.15×0.10 m; (b) 0.20×0.15 m; and (c) 0.25×0.20 m, respectively.

Table 6. Maneuvering performance under different ice floe sizes at fixed 40% concentration.

Case	Ice Floe Size (m)	D_T (m)	180° Time (s)	D (m)
Without ice	—	$4.51L$	35.27	$4.11L$
1	0.15×0.10	$4.24L$	36.16	$3.91L$
2	0.20×0.15	$4.19L$	36.47	$3.84L$
3	0.25×0.20	$3.99L$	37.12	$3.78L$

L is the ship length between perpendiculars.

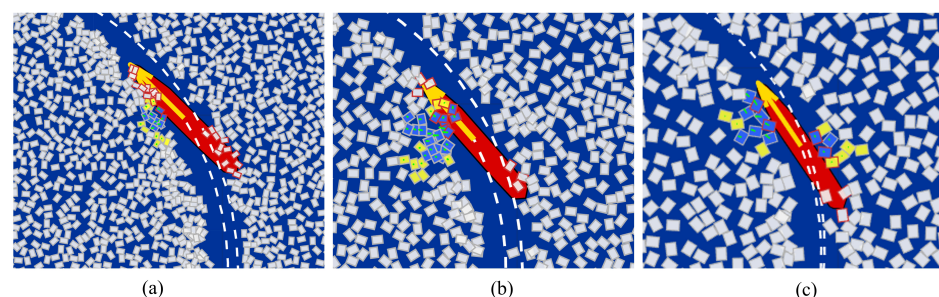


Figure 15. Force-chain structures in the ship–ice contact region for three representative floe sizes: (a) 0.15×0.10 m; (b) 0.20×0.15 m; and (c) 0.25×0.20 m. Larger floes form longer, more stable force chains concentrated near the bow, whereas smaller floes generate more dispersed, short-duration contacts. The yellow arrows indicate the ship’s motion direction, and the red color represents the ship’s hull. The floating ice is color-coded by velocity, with blue representing higher-speed floes and yellow representing lower-speed floes.

Finally, Figure 16 presents the average ice resistance and ice moment experienced by the ship during turning maneuvers in ice fields with different floe sizes. The data further confirm the above analytical conclusions. Compared to the ice moment, ice resistance is more sensitive to changes in the size of the ice floe, with larger floes resulting in a pronounced increase in ice resistance.

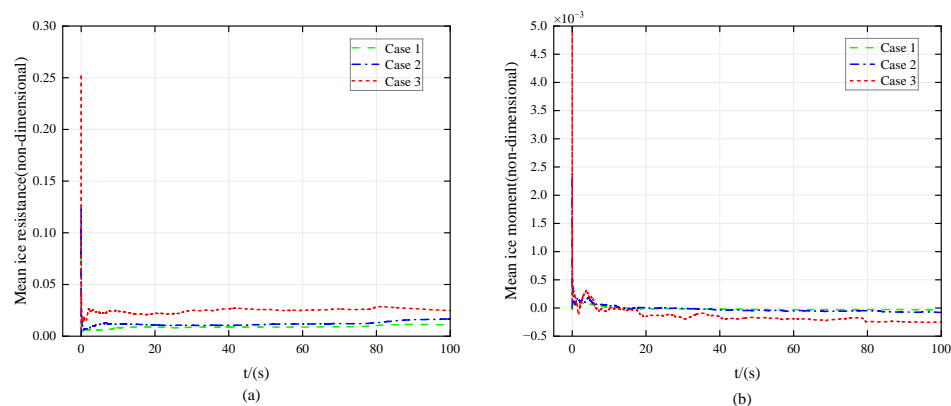


Figure 16. Time histories of the non-dimensional mean ice resistance (a) and mean ice moment (b) acting on the ship during turning maneuvers in ice fields with different floe sizes, under a constant ice concentration of 40%. Cases 1, 2, and 3 correspond to floe sizes of 0.15×0.10 m, 0.20×0.15 m, and 0.25×0.20 m, respectively.

From an operational standpoint, the simulation results provide useful guidance for navigating in broken ice regions. When sailing in high ice concentrations (e.g., $>40\%$), the increased turning resistance and reduced turning radius suggest that vessels should reduce speed in advance and adopt wider initial turning angles to compensate for the restricted maneuverability. For example, in 60% concentration scenarios, the turning time increases noticeably, requiring earlier rudder input to avoid oversteering. Similarly, in environments with large floes, the stronger contact forces and sudden velocity drops indicate a need to limit abrupt heading changes. Maintaining a moderate and steady speed helps avoid excessive impact loads and enables better directional control. These findings suggest that ship operators navigating in marginal ice zones should dynamically adjust maneuvering strategies according to real-time ice concentration and floe size assessments, which can be integrated into intelligent decision-support systems.

3.3. Zig-Zag Maneuvering of the Ship in Broken Ice Fields

The preceding analysis of turning maneuvers indicates that floating ice not only generates forward resistance, thus reducing the ship's speed, but also significantly diminishes the ship's responsiveness to rudder angle changes and constrains its lateral motion freedom. Consequently, performing emergency evasive maneuvers in ice-covered waters is considerably more challenging for non-icebreaking ships than in open water. In this section, typical Zig-Zag maneuver simulations are conducted in floating ice regions to systematically analyze the combined effects of ice concentration and rudder angle amplitude on rudder effectiveness.

3.3.1. Effect of Ice Concentration Zig-Zag Maneuvering

In this section, numerical simulations of Zig-Zag maneuvers are carried out under different ice concentration conditions (0%, 20%, 40%, and 60%) to systematically evaluate the effects of ice concentration on response speed of maneuvering of the ship, response delay, and attitude stability. The results aim to provide theoretical insights into the mechanisms of degradation of the effectiveness of the rudder under complex ice conditions. To ensure fair

comparisons and repeatability of the results, the size of the ice floe size ($0.25\text{ m} \times 0.20\text{ m}$), propeller rotational speed (10.05 rps), and rudder turning rate ($12.0^\circ/\text{s}$) are kept constant throughout the simulations. All tests are performed according to the standard $20^\circ/20^\circ$ Zig-Zag maneuver command, with the initial speed of the ship corresponding to a Froude number of $Fn = 0.15$.

Figure 17 shows the response curves of the heading angle of the ship performing $20^\circ/20^\circ$ Zig-Zag maneuvers under different conditions of ice concentration. The results clearly show that the concentration of ice has a significant impact on the maneuvering performance of the ship. Under ice-free conditions, the ship exhibits a rapid response to the heading angle with a pronounced overshoot angle and sharp rudder reversal behaviour, reflecting the high efficiency of the rudder and strong maneuvering sensitivity. As the ice concentration increases to 20%, 40%, and 60%, the response curves exhibit an increasing lag, and the maximum yaw angle progressively decreases. In particular, at 60% ice concentration, the response delay becomes substantial and the response amplitude is significantly attenuated. This phenomenon indicates that the ice environment weakens the effectiveness of the rudder, delays the build-up of angular velocity, and leads to a marked reduction in maneuvering sensitivity. In addition, the “damping” trend observed in the response curves suggests that the control of the attitude of the ship becomes more delayed and uncertain in high-concentration floating ice conditions.

To further quantify changes in maneuver performance, Table 7 summarizes key maneuver indicators under different conditions of ice concentration. The results show that the first overshoot angle ψ_1 slightly decreases with increasing ice concentration, from 31.41° to 30.04° , indicating a reduction in rudder effectiveness. The maximum yaw rate ($d\psi/dt$) exhibits a more pronounced decreasing trend, declining from $4.986^\circ/\text{s}$ to $4.584^\circ/\text{s}$, which suggests a gradual weakening of the yaw capability of the ship. Variations in response time t_ψ and lag time T_L are relatively small; however, overall fluctuation trends indicate that increasing the concentration of ice introduces certain disturbances to the maneuvering rhythm of the ship.

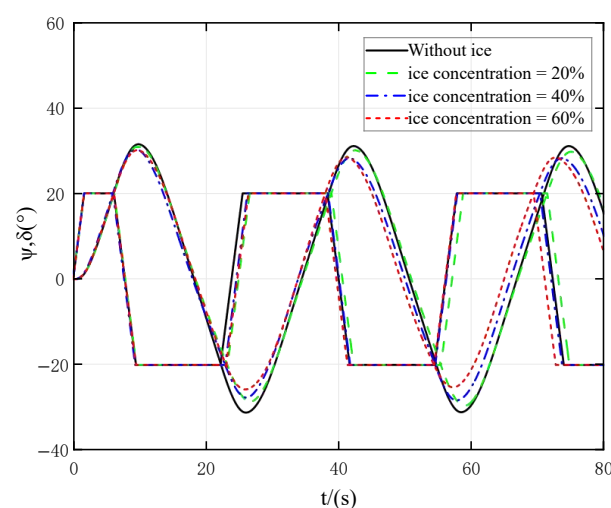


Figure 17. Heading angle response curves of the ship during $20^\circ/20^\circ$ Zig-Zag maneuvers under different ice concentration conditions. The figure illustrates how increasing ice concentration dampens the yaw response, resulting in reduced overshoot and increased time delay.

In addition, Figure 18 illustrates the planar motion trajectories of the ship during the Zig-Zag maneuvers under different ice concentration conditions. In ice-free water, the trajectory exhibits a well-defined symmetrical “Zig-Zag” pattern, characterized by large turning amplitudes and clear turning paths. As the concentration of ice increases to 20%,

40%, and 60%, the trajectories gradually narrow, the turning angles decrease, and the Zig-Zag path tends to straighten, indicating that the resistance to ice significantly weakens the responsiveness to turning of the ship. In high concentration ice fields, the trajectory exhibits pronounced “compression” and “drift lag” phenomena, with some paths even showing asymmetric yaw behaviour, reflecting the increasing influence of ice particle disturbances and non-uniform lateral loads on the ship.

Table 7. Key maneuvering indicators under different ice concentration conditions.

Ice Concentration (%)	Overshoot Angle ψ_1 (°)	Response Time t_ψ (s)	Lag Time T_L (s)	Max Yaw Rate $d\psi/dt$ (°/s)
0	31.412	6.140	4.520	4.986
20	30.985	6.200	4.540	4.871
40	30.194	6.020	4.340	4.756
60	30.044	6.140	4.450	4.584

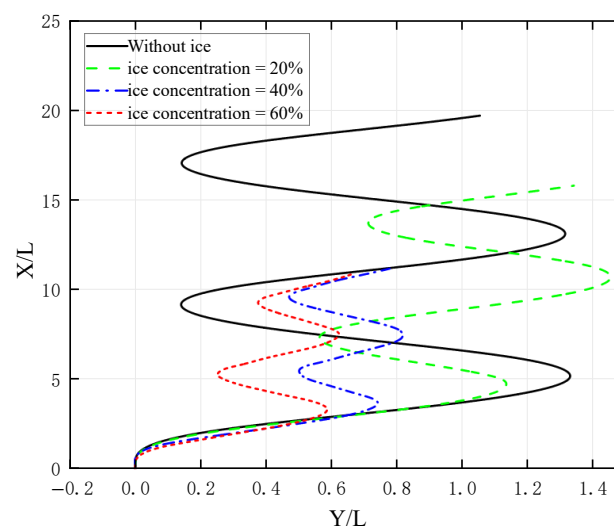


Figure 18. Planar motion trajectories of the ship during 20°/20° Zig-Zag maneuvers under different ice concentration conditions. The results show that higher ice concentrations lead to reduced lateral motion and tighter trajectory envelopes.

In summary, increasing ice concentration exerts a systematic impact on the ship’s Zig-Zag maneuver performance, manifested by a slower rudder response, a reduced turning amplitude, and a diminished attitude control capability. Although the ship can still complete Zig-Zag maneuvers under low-to-moderate ice concentrations (20–40%), a clear trend of rudder effectiveness degradation is already evident. Under 60% ice concentration, maneuvering performance deteriorates significantly, which requires special attention to adapting rudder control timing and attitude stability control strategies.

3.3.2. Effect of Rudder Angle on Zig-Zag Maneuvering

The angle of the rudder is a key control parameter in ship maneuvering. To evaluate the influence of rudder angle on the ship’s Zig-Zag maneuvering response in ice-covered waters, this section conducts numerical simulations under a fixed 40% ice concentration condition with three typical rudder angle settings: 10°/10°, 15°/15°, and 20°/20°. In all test cases, the size of the ice floe is maintained at (0.25 m × 0.20 m), the initial ship speed corresponds to a Froude number of $Fn = 0.15$, and the turning rate of the rudder is set at 12.0°/s, ensuring the consistency and reliability of the comparative results.

Figure 19 presents the response curves of the head angle of the ship in the three rudder angle settings, with the corresponding maneuver performance indicators summarized in

Table 8. The numerical simulation results show that increasing the angle of the rudder significantly improves the yawing capacity of the ship, as evidenced by the larger amplitude of the response curves and the improved sensitivity of the system. In addition, as the angle of the rudder increases, both the response time and the lag time show noticeable changes. Although a larger rudder angle slightly extends the time required to reach the target heading deviation, the lag time is clearly reduced, indicating that enhanced rudder effectiveness facilitates faster initiation of yaw motion and a more responsive system. Furthermore, the yaw rate response curves shown in Figure 20 provide additional information on the dynamic characteristics of the maneuver response. Under conditions of a high angle of rudder, the yaw rate of the ship increases significantly, resulting in a more pronounced response following the rudder commands, with higher turning acceleration and faster attitude adjustment rates. However, this also makes the ship more susceptible to disturbances induced by ice moments, leading to higher-frequency attitude oscillations.

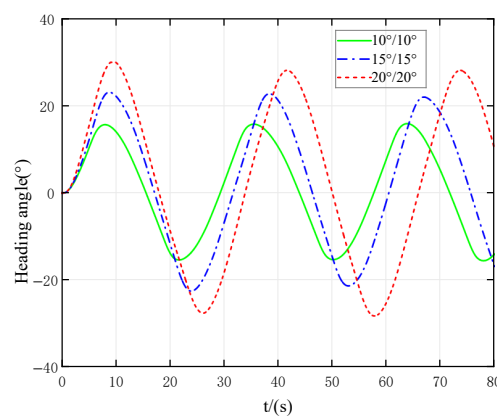


Figure 19. Heading angle response curves of the ship during Zig-Zag maneuvers under three different rudder angle settings: $10^\circ/10^\circ$, $20^\circ/20^\circ$, and $30^\circ/30^\circ$. Larger rudder angles result in faster heading response and increased overshoot.

Table 8. Comparison of Zig-Zag maneuvering indicators under different rudder angle settings.

Rudder Angle ($^\circ$)	Overshoot Angle ϕ_1 ($^\circ$)	Response Time t_ϕ (s)	Lag Time T_L (s)
10/10	15.664	4.980	5.630
15/15	23.115	8.140	5.030
20/20	29.961	8.940	4.540

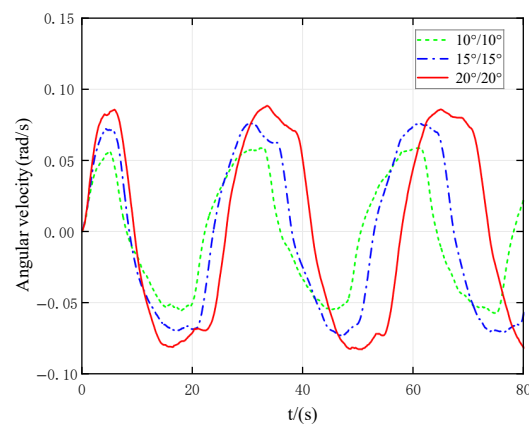


Figure 20. Yaw rate response curves of the ship under three rudder angle settings: $10^\circ/10^\circ$, $15^\circ/15^\circ$, and $20^\circ/20^\circ$. Higher rudder angles result in a sharper and earlier peak yaw rate, indicating improved turning effectiveness and quicker maneuver initiation.

In general, larger rudder angles provide stronger rudder-induced excitation and significantly improve maneuvering sensitivity, but they may also introduce more intense dynamic responses and increased path uncertainty. In complex floating ice environments, maneuvering strategies should carefully balance “response speed” and “dynamic stability” to select an appropriate rudder angle amplitude, thereby ensuring safe and controllable course adjustments.

4. Conclusions

This study systematically investigated the maneuvering performance of non-icebreaking ships in floating ice regions. A numerical simulation framework was established by coupling the MMG ship maneuvering model with NDEM, enabling the simulation of ship maneuvering behaviour in floating ice environments. The effects of ice concentration, ice floe size, and rudder angle on the maneuvering performance of non-icebreaking ships were thoroughly analyzed. The main conclusions are as follows.

- (1) An efficient and robust coupled MMG-NDEM model was developed that is capable of effectively simulating complex dynamic interactions between the ship and floating ice. The model incorporates efficient collision detection techniques and integrates NDEM to compute ice resistance and ice-induced moments in real time, accurately capturing the physical processes of collision and friction between the ship and the ice.
- (2) Numerical simulations confirmed the significant influence of ice concentration on ship maneuvering performance. As the ice concentration increases from 0% to 60%, the turning diameter of the ship decreases from 4.11L to 3.21L, and the steady turning speed drops by approximately 53%. Meanwhile, the time required to complete a 180° turning maneuver increases from 35.27 s to 38.16 s. These results demonstrate that higher ice concentration markedly impairs maneuvering sensitivity, leading to a substantial contraction of the turning path and increased resistance to heading changes.
- (3) The study revealed that ice floe size significantly impacts ship maneuvering performance. As the floe size increases from 0.15 m × 0.10 m to 0.25 m × 0.20 m, the ship's turning diameter decreases from 3.91L to 3.78L, and the time required for a 180° turn increases from 36.16 s to 37.12 s. Larger ice floes tend to form more stable and extended force chain structures, which impose greater longitudinal resistance and lateral constraints on the hull, resulting in reduced turning radius and maneuvering speed. In contrast, smaller floes generate more frequent but short-lived disturbances, offering weaker constraints and thus leading to a comparatively larger turning path.
- (4) Zig-Zag maneuver simulations in floating ice regions were conducted to assess the influence of rudder angle variations on ship maneuverability. As the rudder angle increased from 10°/10° to 20°/20°, the first overshoot angle rose significantly from 15.664° to 29.961°, indicating enhanced yaw responsiveness and maneuvering sensitivity. Concurrently, the response time increased from 4.980 s to 8.940 s, and the system exhibited more pronounced dynamic fluctuations. Notably, the lag time T_L decreased from 5.630 s to 4.540 s, suggesting a faster onset of directional response but also highlighting increased instability associated with higher rudder amplitudes. These results underscore the necessity of optimizing rudder angle selection in complex ice conditions to achieve a trade-off between maneuvering effectiveness and directional stability.

This study provides valuable guidance for the navigation of non-icebreaking ships in floating ice regions. It is recommended that route planning prioritizes avoiding high ice concentration areas (>60%) to mitigate maneuvering risks, while favoring transit through low-to-moderate ice concentrations. Additionally, rudder angles should be dynamically adjusted according to ice conditions: larger angles can enhance maneuverability in low-

to-moderate ice fields, whereas smaller angles can improve heading stability in high-density ice. In complex ice environments, maintaining heading stability should take precedence over frequent course adjustments, and a smooth, gradual maneuvering strategy is recommended to ensure safe and controllable navigation.

Although an efficient and robust coupled MMG-NDEM model was developed and used to systematically analyze the effects of floating ice on ship maneuvering performance, several limitations remain. The current model is based on two-dimensional, three-degree-of-freedom dynamics and does not account for six-degree-of-freedom motion coupling. The ice field was modelled using idealized rectangular floes, which do not fully represent the multiscale characteristics of natural ice fields. Some ice–ship contact parameters were empirically selected and require further optimisation. In addition, complex hydrodynamic effects and highly coupled propeller–ice interactions were not considered.

Future research will aim to extend the present model to full six-degree-of-freedom (6-DOF) simulations, thereby incorporating pitch, roll, and heave motions in addition to surge, sway, and yaw. Moreover, multiscale three-dimensional ice fields with realistic floe geometries and thickness distributions will be implemented, along with fully coupled hydrodynamic interactions among the propeller, rudder, and ice. To enhance engineering applicability, future developments will also include full-scale validation using sea trial data and systematic uncertainty quantification. Overall, this study provides a solid foundation for advancing the analysis of the maneuvering performance of non-icebreaking ships in floating-ice environments and offers concrete directions for achieving higher-fidelity and engineering-ready simulations.

Author Contributions: Conceptualization, D.W., L.Z., Z.Z. and X.C.; Data curation, D.W.; Formal analysis, L.Z.; Funding acquisition, D.W., Z.Z. and X.C.; Investigation, X.C.; Methodology, D.W.; Resources, Z.Z.; Software, L.Z.; Supervision, Z.Z.; Validation, D.W., L.Z. and Z.Z.; Visualization, L.Z.; Writing—original draft, D.W. and L.Z.; Writing—review & editing, L.Z. All authors have read and agreed to the published version of the manuscript.

Funding: This research was funded by the Special Project on Key Technologies and Equipment for the Deep Sea and Polar Regions (Grant No. 2024YFC2816600).

Institutional Review Board Statement: Not applicable.

Informed Consent Statement: Not applicable.

Data Availability Statement: Data are contained within the article.

Conflicts of Interest: The authors declare no conflicts of interest.

Abbreviations

The following abbreviations are used in this manuscript:

MMG	Maneuvering Modeling Group
NSR	Northern Sea Route
DEM	Discrete Element Method
FEM	Finite Element Method
SPH	Smoothed Particle Hydrodynamics
BEM	Boundary Element Method
MPM	Material Point Method
NDEM	Non-Smooth Discrete Element Method
CFD	Computational Fluid Dynamics
MIZ	Marginal Ice Zone
DOF	Degree of Freedom
PMM	Planar Motion Mechanism

CMT	Circular Motion Tests
GJK	Gilbert–Johnson–Keerthi (algorithm)
SAP	Sweep and Prune (algorithm)
AABB	Axis-Aligned Bounding Box
RK4	Fourth-Order Runge–Kutta Method

References

1. Kujala, P.; Goerlandt, F.; Way, B.; Smith, D.; Yang, M.; Khan, F.; Veitch, B. Review of risk-based design for ice-class ships. *Mar. Struct.* **2019**, *63*, 181–195. [\[CrossRef\]](#)
2. Chen, X.; Wei, C.; Xin, Z.; Zhao, J.; Xian, J. Ship detection under low-visibility weather interference via an ensemble generative adversarial network. *J. Mar. Sci. Eng.* **2023**, *11*, 2065. [\[CrossRef\]](#)
3. Chen, X.; Ma, F.; Wu, Y.; Han, B.; Luo, L.; Biancardo, S.A. MFMDepth: MetaFormer-based monocular metric depth estimation for distance measurement in ports. *Comput. Ind. Eng.* **2025**, *207*, 111325. [\[CrossRef\]](#)
4. Guo, R.; Xiao, G.; Zhang, C.; Li, Q. A study on influencing factors of port cargo throughput based on multi-scale geographically weighted regression. *Front. Mar. Sci.* **2025**, *12*, 1637660. [\[CrossRef\]](#)
5. Wang, T.; Xiao, G.; Li, Q.; Biancardo, S.A. The impact of the 21st-Century Maritime Silk Road on sulfur dioxide emissions in Chinese ports: Based on the difference-in-difference model. *Front. Mar. Sci.* **2025**, *12*, 1608803. [\[CrossRef\]](#)
6. Xiao, G.; Amamoo-Otoo, C.; Wang, T.; Li, Q.; Biancardo, S.A. Evaluating the impact of ECA policy on sulfur emissions from the five busiest ports in America based on difference in difference model. *Front. Mar. Sci.* **2025**, *12*, 1609261. [\[CrossRef\]](#)
7. Lewis, J.W.; Edwards, R.Y., Jr. *Methods for Predicting Icebreaking and Ice Resistance Characteristics of Icebreakers*; The National Academies of Sciences, Engineering, and Medicine: Washington, DC, USA, 1970.
8. Lindquist, A. Straightforward method for calculation of ice resistance of ships. In Proceedings of the POAC'89, Lulea, Sweden, 12–16 June 1989.
9. Riska, K.; Patey, M.; Kishi, S.; Kamesaki, K. Influence of ice conditions on ship transit times in ice. In Proceedings of the International Conference on Port and Ocean Engineering Under Arctic Conditions, Ottawa, ON, Canada, 12–17 August 2001.
10. Jeong, S.Y.; Choi, K.; Kim, H.S. Investigation of ship resistance characteristics under pack ice conditions. *Ocean Eng.* **2021**, *219*, 108264. [\[CrossRef\]](#)
11. Huang, L.; Li, Z.; Ryan, C.; Ringsberg, J.W.; Pena, B.; Li, M.; Ding, L.; Thomas, G. Ship resistance when operating in floating ice floes: Derivation, validation, and application of an empirical equation. *Mar. Struct.* **2021**, *79*, 103057. [\[CrossRef\]](#)
12. Han, K.; Zhang, Y.; Ye, L.; Guo, C.; Wang, C. Experimental research on propeller-ice contact process and prediction of extreme ice load. *Ocean Eng.* **2023**, *287*, 115912. [\[CrossRef\]](#)
13. Zhou, L.; Gu, Y.; Ding, S.; Liu, R. Prediction of ice-resistance distribution for R/V Xuelong using measured sea-ice parameters. *Water* **2022**, *14*, 517. [\[CrossRef\]](#)
14. Jeon, S.; Kim, Y. Numerical simulation of level ice–structure interaction using damage-based erosion model. *Ocean Eng.* **2021**, *220*, 108485. [\[CrossRef\]](#)
15. Kim, J.H.; Kim, Y.; Kim, H.S.; Jeong, S.Y. Numerical simulation of ice impacts on ship hulls in broken ice fields. *Ocean Eng.* **2019**, *182*, 211–221. [\[CrossRef\]](#)
16. Wang, C.; Hu, X.; Tian, T.; Guo, C.; Wang, C. Numerical simulation of ice loads on a ship in broken ice fields using an elastic ice model. *Int. J. Nav. Archit. Ocean Eng.* **2020**, *12*, 414–427. [\[CrossRef\]](#)
17. Kim, J.; Yoon, D.H.; Choung, J. Numerical study of ship hydrodynamics on ice resistance during ice sheet breaking. *Ocean Eng.* **2024**, *308*, 118285. [\[CrossRef\]](#)
18. Xing, W.; Cong, S.; Ling, X.; Li, X.; Cheng, Z.; Tang, L. Numerical study of ice loads on different interfaces based on cohesive element formulation. *Sci. Rep.* **2023**, *13*, 14434. [\[CrossRef\]](#)
19. Makarov, O.; Bekker, A.; Li, L. Comparative analysis of numerical methods for the modeling of ice–structure interaction problems. *Contin. Mech. Thermodyn.* **2022**, *34*, 1621–1639. [\[CrossRef\]](#)
20. Li, Z.; Liu, Y.; Sun, S.; Lu, Y.; Ji, S. Analysis of ship maneuvering performances and ice loads on ship hull with discrete element model in broken-ice fields. *Chin. J. Theor. Appl. Mech.* **2013**, *45*, 868–877.
21. Polojärvi, A.; Tuhkuri, J.; Gong, H. Comparison of full-scale and DEM simulation data on ice loads due to floe fields on a ship hull. In Proceedings of the International Conference on Port and Ocean Engineering Under Arctic Conditions, Moscow, Russia, 14–18 June 2021; Luleå Tekniska Universitet: Luleå, Sweden, 2021.
22. Mucha, P. Fully-coupled CFD-DEM for simulations of ships advancing through brash ice. In Proceedings of the SNAME Maritime Convention, Tacoma, WA, USA, 30 October–2 November 2019; SNAME: Alexandria, VA, USA, 2019; p. D023S004R005.

23. Huang, L.; Tuhkuri, J.; Igrec, B.; Li, M.; Stagonas, D.; Toffoli, A.; Cardiff, P.; Thomas, G. Ship resistance when operating in floating ice floes: A combined CFD&DEM approach. *Mar. Struct.* **2020**, *74*, 102817. [\[CrossRef\]](#)
24. Tang, X.; Zou, M.; Zou, Z.; Li, Z.; Zou, L. A parametric study on the ice resistance of a ship sailing in pack ice based on CFD-DEM method. *Ocean Eng.* **2022**, *265*, 112563. [\[CrossRef\]](#)
25. Hu, B.; Liu, L.; Wang, D.Y. Prediction of performance of a non-icebreaking ship in marginal ice zone. *J. Hydrodyn.* **2022**, *34*, 315–328. [\[CrossRef\]](#)
26. Xie, C.; Zhou, L.; Ding, S.; Liu, R.; Zheng, S. Experimental and numerical investigation on self-propulsion performance of polar merchant ship in brash ice channel. *Ocean Eng.* **2023**, *269*, 113424. [\[CrossRef\]](#)
27. Xue, Y.; Zhong, K.; Ni, B.Y.; Li, Z.; Bergström, M.; Ringsberg, J.W.; Huang, L. A combined experimental and numerical approach to predict ship resistance and power demand in broken ice. *Ocean Eng.* **2024**, *292*, 116476. [\[CrossRef\]](#)
28. Zou, M.; Tang, X.J.; Zou, L.; Zou, Z.J.; Zhang, X.S. Numerical investigations of the restriction effects on a ship navigating in pack-ice channel. *Ocean Eng.* **2024**, *305*, 117968. [\[CrossRef\]](#)
29. Mierke, D.; Janssen, D.; Rung, T. GPU-accelerated large-eddy simulation of ship-ice interactions. In Proceedings of the MARINE VI: VI International Conference on Computational Methods in Marine Engineering, Rome, Italy, 15–17 June 2015; CIMNE: Barcelona, Spain, 2015; pp. 850–861.
30. Lubbad, R.; Løset, S. A numerical model for real-time simulation of ship–ice interaction. *Cold Reg. Sci. Technol.* **2011**, *65*, 111–127. [\[CrossRef\]](#)
31. van den Berg, M.; Lubbad, R.; Løset, S. An implicit time-stepping scheme and an improved contact model for ice-structure interaction simulations. *Cold Reg. Sci. Technol.* **2018**, *155*, 193–213. [\[CrossRef\]](#)
32. Yang, B.; Sun, Z.; Zhang, G.; Wang, Q.; Zong, Z.; Li, Z. Numerical estimation of ship resistance in broken ice and investigation on the effect of floe geometry. *Mar. Struct.* **2021**, *75*, 102867. [\[CrossRef\]](#)
33. Zhan, D.; Molyneux, D. 3-dimensional numerical simulation of ship motion in pack ice. In Proceedings of the International Conference on Offshore Mechanics and Arctic Engineering, Rio de Janeiro, Brazil, 1–6 July 2012; American Society of Mechanical Engineers: New York, NY, USA, 2012; Volume 44939, pp. 407–414.
34. Zhou, Q.; Peng, H.; Qiu, W. Numerical investigations of ship–ice interaction and maneuvering performance in level ice. *Cold Reg. Sci. Technol.* **2016**, *122*, 36–49. [\[CrossRef\]](#)
35. Di, S.C.; Wang, Q.; Xue, Y.Z.; Li, J.L. Manoeuvrability Analysis of an Icebreaker Based on Discrete Element Metho. *Eng. Mech.* **2018**, *35*, 249–256.
36. Yang, B.; Zhang, G.; Rao, H.; Wang, S.; Yang, B.; Sun, Z. Numerical simulation of the maneuvering performance of ships in broken ice area. *Ocean Eng.* **2024**, *294*, 116783. [\[CrossRef\]](#)
37. Yasukawa, H.; Sakuno, R. Application of the MMG method for the prediction of steady sailing condition and course stability of a ship under external disturbances. *J. Mar. Sci. Technol.* **2020**, *25*, 196–220. [\[CrossRef\]](#)
38. Yasukawa, H. Simulations of ship maneuvering in waves (1 st report: Turning motion). *J. Jpn. Soc. Nav. Archit. Ocean Eng.* **2006**, *4*, 127–136.
39. Yasukawa, H.; Yoshimura, Y. Introduction of MMG standard method for ship maneuvering predictions. *J. Mar. Sci. Technol.* **2015**, *20*, 37–52. [\[CrossRef\]](#)
40. Zhang, W.; Zou, Z.J.; Deng, D.H. A study on prediction of ship maneuvering in regular waves. *Ocean Eng.* **2017**, *137*, 367–381. [\[CrossRef\]](#)
41. Lee, J.H.; Kim, Y. Study on steady flow approximation in turning simulation of ship in waves. *Ocean Eng.* **2020**, *195*, 106645. [\[CrossRef\]](#)
42. Zhang, Z.; Zhang, X.; Zhang, H.; Bu, S.; Zou, Z. Numerical evaluation of turning performance of ships in regular and long-crested irregular waves. *Ocean Eng.* **2024**, *308*, 118201. [\[CrossRef\]](#)
43. Sharkawy, A.N.; Koustoumpardis, P.N.; Aspragathos, N. Human–robot collisions detection for safe human–robot interaction using one multi-input–output neural network. *Soft Comput.* **2020**, *24*, 6687–6719. [\[CrossRef\]](#)
44. Mahmoud, K.H.; Sharkawy, A.N.; Abdel-Jaber, G. Development of safety method for a 3-DOF industrial robot based on recurrent neural network. *J. Eng. Appl. Sci.* **2023**, *70*, 44. [\[CrossRef\]](#)
45. Stewart, D.E.; Trinkle, J.C. An implicit time-stepping scheme for rigid body dynamics with inelastic collisions and coulomb friction. *Int. J. Numer. Methods Eng.* **1996**, *39*, 2673–2691. [\[CrossRef\]](#)
46. Yulmetov, R.; Lubbad, R.; Løset, S. Planar multi-body model of iceberg free drift and towing in broken ice. *Cold Reg. Sci. Technol.* **2016**, *121*, 154–166. [\[CrossRef\]](#)
47. Kim, H.; Daley, C.; Colbourne, B. A numerical model for ice crushing on concave surfaces. *Ocean Eng.* **2015**, *106*, 289–297. [\[CrossRef\]](#)
48. Metrikin, I. A software framework for simulating stationkeeping of a vessel in discontinuous ice. *Model. Identif. Control* **2014**, *35*, 211–246. [\[CrossRef\]](#)

49. Zhang, Z.; Li, Z.; Du, Y.; Jiang, X. A rapid motion forecast strategy for ships in waves using seakeeping and maneuvering modules. *Ocean Eng.* **2024**, *309*, 118539. [[CrossRef](#)]
50. Yasukawa, H. Simulations of ship maneuvering in waves: 2nd report: Zig-zag and stopping maneuvers. *J. Jpn. Soc. Nav. Archit. Ocean Eng.* **2008**, *7*, 163–170. [[CrossRef](#)]
51. Lu, W.; Lubbad, R.; Løset, S. In-plane fracture of an ice floe: A theoretical study on the splitting failure mode. *Cold Reg. Sci. Technol.* **2015**, *110*, 77–101. [[CrossRef](#)]
52. Lu, W.; Lubbad, R.; Løset, S. Out-of-plane failure of an ice floe: Radial-crack-initiation-controlled fracture. *Cold Reg. Sci. Technol.* **2015**, *119*, 183–203. [[CrossRef](#)]
53. Lu, W.; Lubbad, R.; Løset, S.; Kashafutdinov, M. Fracture of an ice floe: Local out-of-plane flexural failures versus global in-plane splitting failure. *Cold Reg. Sci. Technol.* **2016**, *123*, 1–13. [[CrossRef](#)]

Disclaimer/Publisher’s Note: The statements, opinions and data contained in all publications are solely those of the individual author(s) and contributor(s) and not of MDPI and/or the editor(s). MDPI and/or the editor(s) disclaim responsibility for any injury to people or property resulting from any ideas, methods, instructions or products referred to in the content.